Supporting Information

for

Separable *Syn*/*Anti* Dinuclear Co(II) Macrocycles as Robust High-Performance paraCEST MRI Probes

Xin Guo,[a] Maosong Qiu,[bc] Jiesheng Hu,[a] Shizhen Chen,[bc] Meng Yu,*[a] Lei Zhang,*[bc] Jun Tao*[a]

[a] Key Laboratory of Cluster Science of Ministry of Education, School of Chemistry and Chemical Engineering, Liangxiang Campus, Beijing Institute of Technology, Beijing 102488, P. R. China
E-mail: mengyu@bit.edu.cn, taojun@bit.edu.cn

[b] State Key Laboratory of Magnetic Resonance Spectroscopy and Imaging, National Center for Magnetic Resonance in Wuhan, Wuhan Institute of Physics and Mathematics, Innovation Academy for Precision Measurement Science and Technology, Chinese Academy of Sciences, Wuhan 430071, P. R. China.
E-mail: leizhang@apm.ac.cn

[c] University of Chinese Academy of Sciences, Beijing 100049, P. R. China.

Contents

1. Materials and Methods

All reagents and deuterated solvents were used as purchased without further purification. All ^{1}H NMR data were recorded on Bruker Avance spectrometers (400 MHz or 500 MHz) at 298 K. The CEST spectra were recorded using a Bruker 400 WB (400 MHz), while the relaxation time measurements were conducted on a Bruker Avance (500 MHz). High resolution mass spectrometry (HR-MS) data were obtained on an Agilent Q-TOF 6520 mass spectrometer. UV–vis absorption spectra were recorded using a Shimadzu UV-1900 spectrometer with 1 cm quartz cuvettes. Fourier transform infrared (FT-IR) spectra were recorded on a Bruker ALPHA II spectrometer in the range of 400–4000 cm^{-1}. Elemental analyses (C, H, N, O) were performed on a Thermo FLASH2000 analyzer.

X-Ray Structure Determination.

The single-crystal X-ray diffraction data of **1** were recorded on a Rigaku Oxford XtaLAB PRO diffractometer with graphite-monochromated Mo *Kα* radiation (λ = 0.71073 Å). The crystal data of **2, 1′,** and **2′** were collected with a Bruker/ARINAX MD2 diffractometer equipped with a MarCCD-300 detector (λ = 0.77484 Å) at the BL17B beamline station of the Shanghai Synchrotron Radiation Facility (SSRF). The structures were solved by direct methods and further refined by full-matrix least-squares techniques on F^2 with SHELX program.[1] The hydrogen atom positions were fixed geometrically at calculated distances and allowed to ride on the parent atoms. Attempts to define the highly disordered solvent molecules were unsuccessful, so the structure was refined using the PLATON SQUEEZE procedure.[2] Thus, the solvent molecules in crystal **2** were identified with the assistance of elemental analysis. Crystallographic data have been deposited with the CCDC no.2531364-2531367.

NMR Spectroscopy.

Chemical shifts (δ) are reported in ppm, with coupling constants (J) given in Hz. Residual signals of deuterated solvents served as references (D_2O at 4.79 ppm). All ^{1}H NMR experiments were carried out at 298 K unless otherwise noted. NMR samples were prepared and stored under a nitrogen atmosphere to avoid oxidation. For the samples in HEPES buffer or fetal bovine serum (FBS) at various pH values, D_2O was placed in an inner capillary within each NMR tube for field locking.

Kinetic experiments.

The samples of **1** were subjected to isothermal heating at 37, 55, and 70 °C, respectively, with periodic sampling conducted at 1 h intervals. The molar ratio of **1** to **2** in the reaction mixture was quantified using ^{1}H NMR (Bruker Avance spectrometers 400 MHz). On the basis of the acquired data, the temperature-dependent reaction rate constants (k) were computed. Thereafter, these kinetic data were fitted to the Eyring equation by plotting the reaction rate

constant *k* against the reciprocal of the thermodynamic temperature (1/*T*) for linear regression analysis. Ultimately, the activation thermodynamic parameters $\Delta H^{\neq}$ (activation enthalpy) and $\Delta S^{\neq}$ = (activation entropy) of the reaction were obtained, and the Gibbs free energy change $\Delta G^{\neq}$ at 298 K was further deduced therefrom.

Solution Magnetic Properties.

Measurements were acquired on a 400 MHz Bruker AVANCE spectrometer at 37 °C (310 K). The compounds (5−10 mM) were dissolved in an aqueous HEPES buffer containing 50 mM HEPES, 100 mM NaCl, and 5% (v/v) tert-butanol. Samples were prepared under a nitrogen atmosphere to prevent degradation by air oxidation. The resulting solutions were placed in NMR tubes, with an internal reference solution consisting of the same solvent mixture but without the paramagnetic compounds to be characterized. The solution magnetic moments of compounds were determined based on Evans' method.[3] A degassed solution of the 5−10 mM metal complex in D_2O containing 5% (v/v) tert-butanol was placed in an NMR coaxial tube, with 5% tert-butanol in D_2O as the reference. The effective magnetic moment (μ_{eff}) was calculated at 298 K by using the equations given below.

$$\chi_g = \frac{3\Delta f}{4\pi f m} + \chi_0 + \frac{\chi_0(d_0 - d_s)}{m} \qquad \text{(eq. S1)}$$

$$\mu_{eff} = 2.84\sqrt{\chi_M T} \qquad \text{(eq. S2)}$$

Δf stands for the proton chemical shift of *tert*-butanol in frequency (Hz) between the reference and paramagnetic sample, the spectrometer frequency (f) in Hz, the mass of the substance per mL of the solution (m), and the mass susceptibility of deuterium oxide (χ_0 = −0.6466 × 10^{-6} cm^3 g^{-1}), the density of solvent (d_0) in g·cm^{-3}, and the density of solvent (d_s) in g·cm^{-3}. The last term in eq. S2 is neglected. The molar susceptibility (χ_M) is the product of χ_g times the molecular weight of metal complex.[4] The experiment was repeated two times and averaged.

Solid-State Magnetic Measurements.

Magnetic susceptibility measurements were performed on a Quantum Design MPMS XL7 magnetometer. Powdered samples of **1** or **2** were loaded into gelatin capsules and inserted into straws for SQUID analysis. Variable-temperature magnetic susceptibilities were measured from 2–300 K at 5000 Oe, with a temperature ramp rate of 2 K·min^{-1}. Variable-field magnetic

susceptibilities were measured at 3, 5, 7, 10 K for applied fields ranging from 0–7 T. Diamagnetic correction was performed by deducting empty sample holder and Pascal's constants.[5]

CEST Experiments.

The chemical exchange saturation transfer (CEST) experiments were carried out on a Bruker 400 WB (400 MHz) superconducting nuclear magnetic resonance spectrometer (9.4 T) at a temperature of 37 °C. The CEST samples were compounds **1** and **2** with a concentration of 10 mM, which were dissolved separately in aqueous buffer solutions containing 50 mM HEPES and 100 mM NaCl. The pH of NMR samples was adjusted to the target value using 1 M NaOH or 1 M HCl, and measured with a pH electrode before ^{1}H NMR and CEST data collection. A capillary filled with 100% D_2O was placed in a 5 mm NMR sample tube for field locking.

The experimental protocol for obtaining CEST spectra (*Z*-spectra) is as follows: The frequency of the direct saturation value of the water signal was set to 0 ppm. A presaturation pulse with a power level of 20 μT (B_1) was applied for 4 s, and ^{1}H NMR spectra were collected in the range of −40–120 ppm. The specific ^{1}H NMR acquisition parameters for Sample **1** and Sample **2** are as follows:

1. Sample **1**: The acquisition ranges include 120~80 ppm (acquisition interval: 5 ppm), 80~70 ppm (acquisition interval: 0.5 ppm), 70~20 ppm (acquisition interval: 5 ppm), 20~15 ppm (acquisition interval: 1 ppm), 15~9 ppm (acquisition interval: 0.5 ppm), 9~−5 ppm (acquisition interval: 1 ppm), and −5~−40 ppm (acquisition interval: 5 ppm).

2. Sample **2**: The acquisition ranges include 120~85 ppm (acquisition interval: 5 ppm), 85~72 ppm (acquisition interval: 0.5 ppm), 72~20 ppm (acquisition interval: 5 ppm), 20~16 ppm (acquisition interval: 1 ppm), 16~−5 ppm (acquisition interval: 1 ppm), and −5~−40 ppm (acquisition interval: 5 ppm).

The normalized integral value of the water signal in the obtained spectra was plotted against the frequency offset, and thus the CEST spectra (*Z*-spectra) were obtained. The CEST% value [$(1-M_z/M_0)\times100\%$] is defined as the difference between the decrease in H_2O signal when resonant presaturation is applied and the value obtained by substituting the corresponding frequency into the linear baseline equation.

Exchange rate constants (k_{ex}) were calculated following a previously reported method,[3] where the k_{ex} intercept ($-1/k_{ex}^2$) was obtained from a plot of $M_z/(M_0-M_z)$ against $1/\omega_1^2$ (ω_1 in rad·s^{-1}). ^{1}H NMR spectra were acquired at 37 °C with a 4 s presaturation pulse applied at various power levels ranging from 2–20 μT.

Electrochemical Measurements.

Cyclic voltammetry measurements were conducted on a CHI660E electrochemical

workstation. A standard three-electrode system was employed in the electrochemical cell, consisting of a glassy carbon working electrode, a platinum wire counter electrode, and an Ag/AgCl reference electrode. The supporting electrolyte was HEPES buffer solution (50 mM HEPES, 100 mM NaCl, pH = 7.40). HEPES buffer solutions containing 1 mM of compound **1** or **2** were prepared accordingly. Prior to each measurement, the sample solution was deoxygenated with nitrogen gas for at least 15 minutes. The voltammograms were converted to the normal hydrogen electrode (NHE) reference scale using the conversion factor reported in the literature.[6]

Computational Methods

Density functional theory (DFT) calculations were performed using the ORCA quantum chemistry software version 6.1.0 .[7-9] Using atomic coordinates obtained from the X-ray crystallographic data as a start, complexes **1** and **2** were optimized at the PBE0/def2-TZVP level in water environment using the SMD model[10] and D4 dispersion correction.[11] Frequency calculation on an optimized geometry was performed to ensure a true local minimum on the potential energy surface (PES) by the absence of imaginary frequencies. Gibbs free energies in solution at 298.15 K were calculated using Grimme's quasi-RRHO model[12], combining thermodynamic corrections (G_n), electronic energies (E_{el}), and a 1.89 kcal mol^{-1} correction for standard state conversion from 1 atm to 1 mol L^{-1}. To elucidate the chair↔boat interconversion of **1** and **2** , the Nudged Elastic Band method[13, 14] was employed (using the NEB-TS keyword) to find the transition state. For broken-symmetry calculations, coordinates from crystal structure were directly utilized without further optimization. Scalar relativistic effects were taken into account using Zero-Order Regular Approximation (ZORA) method[15] combined with ZORA-def2-TZVP basis set for all atoms. The RIJCOSX approximations combined with appropriate Ahlrichs auxiliary basis sets were routinely employed to speed up the calculations.[16-18] Tight SCF convergence criteria were used for all calculations. The magnetic exchange coupling constants (J) was calculated using the Yamaguchi formalism according to the following equation where the spin Hamiltonian $\hat{H} = -2J\hat{S}_1 \cdot \hat{S}_2$ is assumed.

$$J\,(1) = -(E_{HS} - E_{BS})/S_{max}{}^{19, 20}$$

$$J\,(2) = -(E_{HS} - E_{BS})/S_{max}(S_{max} + 1)^{21}$$

$$J\,(3) = -(E_{HS} - E_{BS})/(\langle S^2\rangle_{HS} - \langle S^2\rangle_{BS})^{22}$$

E_{HS} and E_{BS} stand for the energies of the high-spin state ($S = 3$) and broken-symmetry state ($S = 0$) of the dinuclear Co(II) complex. The broken-symmetry state corresponds to configuration where three unpaired spin-up, α electrons are localized on one site and three unpaired spin-down, β electrons localized on the other site. $\langle S^2\rangle_{HS}$ and $\langle S^2\rangle_{BS}$ denote the expectation values of the total spin operators for the ferromagnetic and antiferromagnetic spin states, respectively. S_{max} stands for the total spin number of high-spin state.

2. Synthetic Methods

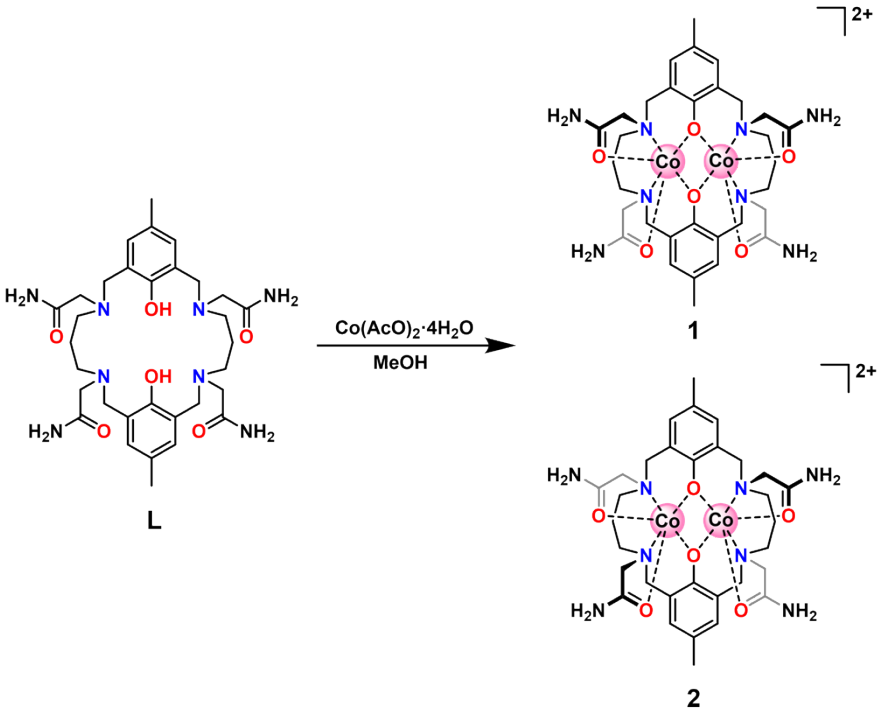

Scheme S1. Synthesis of **1** and **2**.

The synthesis of L followed the experimental protocol reported previously.[23]

L (100 mg, 156 mmol) and $Co(OAc)_2 \cdot 6H_2O$ (85.4 mg, 343 mmol) were added to a 50 mL round-bottom flask. To this, 25 mL of methanol was then added, and the mixture was stirred at ambient temperature for 16 h under nitrogen atmosphere, during which the solution changed from pink to purple-red. Methanol was then removed under vacuum and the crude was purified by reverse phase chromatography using H_2O/MeCN (0.1% HCOOH) as eluent. Product eluted at 20% acetonitrile content and lyophilization afforded a pink powder, which was confirmed to be a mixture of complex 1 and 2 by NMR spectroscopy. Isopropyl ether was diffused into a methanolic solution of the pink powder at 40 °C, following two days, the uniformly grown pink block-shaped crystals on the wall were carefully scraped off, affording complex **1** (13.6 mg, 11.8%). HRMS (ESI^+): Calcd for $[L+2M+2H]^+$ ($C_{32}H_{45}Co_2N_8O_6$) 755.2120, found 378.1106 (86%,$[L+2M+H]^{2+}$), 755.2086 (1.79%, $[L+2M+2H]^+$). Anal. Calcd. for $C_{36}H_{66}Co_2N_8O_{17}$: C, 44.40; H, 6.56; O, 26.05; N, 11.40%. Found: C, 43.73; H, 6.55; O, 26.33; N, 11.17%. UV–vis absorption spectrum (HEPES, pH = 7.35, 25 °C): 301 nm ($\epsilon = 7250\ M^{-1}cm^{-1}$), 380 nm ($\epsilon = 105\ M^{-1}cm^{-1}$), 590 nm ($\epsilon = 41.3\ M^{-1}cm^{-1}$). FT-IR (ATR, cm−1): 1653 (m); 1612(m); 1543 (s); 1470 (s); 1388 (s); 1323 (m); 1296 (s); 1234(s); 1169 (s); 1099 (m); 1053 (m); 1026 (m); 1011 (m); 972 (s); 883 (m); 864 (m); 799 (s); 748 (m); 675 (s); 640 (s); 583 (s); 486 (s); 447 (m).

The remaining solution was purged with nitrogen for 5–10 min, and fresh isopropyl ether was then added to continue crystal growth. After three days, the single crystals (rod-shaped, clustered, and flocculent) were collected, which was confirmed to be complex **2** (46 mg, 34%) by ^{1}H NMR spectroscopy and single-crystal X-ray diffraction result. HRMS (ESI$^+$): Calcd for [L+2M+2H]$^+$ ($C_{32}H_{45}Co_2N_8O_6$) 755.2120, found 378.1106 (100%, [L+2M+H]$^{2+}$), 755.2086 (22%, [L+2M+2H]$^+$). Anal. Calcd. for $C_{36}H_{66}Co_2N_8O_{17}$: C, 43.20; H, 6.65; O, 27.18; N, 11.20%. Found: C, 43.88; H, 6.35; O, 25.67; N, 11.14%. UV–vis absorption spectrum (HEPES, pH = 7.35, 25 °C): 301 nm ($\epsilon = 7250\ M^{-1}cm^{-1}$), 380 nm ($\epsilon = 105\ M^{-1}cm^{-1}$), 590 nm ($\epsilon = 41.3\ M^{-1}cm^{-1}$). FT-IR (ATR, cm−1): 1658(s); 1609 (m); 1547 (s); 1470 (s); 1446 (s); 1393 (s); 1323 (m); 1242 (s); 1161 (s); 1103 (m); 1030 (m); 972 (m); 957 (m); 918 (m); 883(m); 864 (s); 795 (s); 752 (m); 1296 (s); 686 (s); 644 (s); 583 (s); 567 (s); 497 (s); 439 (m).

3. Additional Tables

Table S1. X-ray crystallography data for complexes **1** and **2**.

	1	**2**
CCDC number	2531364	2531365
Empirical formula	$C_{46}H_{62}Co_2N_6O_{13}$	$C_{36}H_{52}Co_2N_8O_{10}$
Formula weight	962.38	874.71
Temperature (K)	100.03(10)	100.15
Crystal system	Triclinic	Monoclinic
Space group	$P\bar{1}$	*C*2/*c*
a (Å)	12.1854(2)	21.9022(16)
b (Å)	12.8834(3)	17.6776(16)
c (Å)	16.3273(3)	14.8986(16)
α (°)	102.397(2)	90
β (°)	102.207(2)	128.698(7)
γ (°)	105.719(2)	90
V (Å^3)	2308.61(8)	4502.0(8)
Z	2	4
ρ_{calcd} (g/cm^3)	1.384	1.291
μ (mm^{-1})	0.787	0.735
F (000)	952.0	1832.0
θ_{max} (deg)	29.9380	27.77
completeness (%)	99.5	91.3
no. of. rflns collected	42991	24732
no. of. indep rflns	11561	4478
Goodness of fit on F^2	1.066	1.051
Final *R* indexes [$I \geq 2\sigma(I)$]	$R_1 = 0.0617$, $wR_2 = 0.1888$	$R_1 = 0.0801$, $wR_2 = 0.2202$
Final *R* indexes [all	$R_1 = 0.0667$, $wR_2 = 0.1928$	$R_1 = 0.1114$, $wR_2 = 0.2517$

data]			

[a] $R1 = \Sigma||F0| - |FC||/\Sigma|F0|$. [b] $wR2 = [\Sigma w(F_0^2 - F_C^2)^2/\Sigma w(F_0^2)^2]^{1/2}$.

Table S2. X-ray crystallography data for complexes **1′** and **2′**.

	1′	**2′**
CCDC number	2531366	2531367
Empirical formula	$C_{32}H_{46}Cl_2Co_2N_8O_6$	$C_{64}H_{94.68}Cl_4Co_4N_{16}O_{13.34}$
Formula weight	827.53	1679.21
Temperature (K)	100.15	100.15
Crystal system	Trigonal	Monoclinic
Space group	$P3_221$	$C2/c$
a (Å)	14.360	18.7447(7)
b (Å)	14.360	21.4945(8)
c (Å)	36.450	20.7934(8)
α (°)	90	90
β (°)	90	102.820(4)
γ (°)	120	90
V (Å^3)	6509.3	8169.0(5)
Z	6	4
ρ_{calcd} (g/cm^3)	1.267	1.365
μ (mm^{-1})	0.862	0.994
F (000)	2580.0	3494.0
θ_{max} (deg)	42.21	30.0600
completeness (%)	99.8	99.6
no. of. rflns collected	103180	41533
no. of. Indep rflns	11990	10471
Goodness of fit on F^2	1.049	1.042
Final R indexes [$I \geq 2\sigma(I)$]	$R_1 = 0.0488$, $wR_2 = 0.1496$	$R_1 = 0.0519$, $wR_2 = 0.1264$
Final R indexes [all data]	$R_1 = 0.0496$, $wR_2 = 0.1512$	$R_1 = 0.0630$, $wR_2 = 0.1315$

[a] $R1 = \Sigma||F0| - |FC||/\Sigma|F0|$. [b] $wR2 = [\Sigma w(F_0^2 - F_C^2)^2/\Sigma w(F_0^2)^2]^{1/2}$.

Table S3. Selected bond lengths (Å) and bond angles (°) and distortion parameters for complexes **1**, **2**, **1′**, and **2′**.

1				**2**	
Co1–O1	2.0232(11)	Co2–O4^2	2.0422(11)	Co1–O2	2.060(4)
Co1–O1^1	2.0343(11)	Co2–O4	2.0409(12)	Co1–O3	2.184(3)
Co1–O3^1	2.1773(11)	Co2–O6^2	2.1363(11)	Co1–O1	2.046(4)
Co1–O2	2.1574(11)	Co2–O5	2.1288(12)	Co1–O4	2.126(4)
Co1–N2^1	2.1174(13)	Co2–N5	2.1480(14)	Co1–N1	2.171(5)

Co1–N1	2.1465(14)	Co2–N6^{2}	2.1503(14)	Co1–N2	2.138(4)
O1–Co1–O1^{1}	82.87(5)	O4–Co2–O4^{2}	82.63(5)	O2–Co1–N2	164.86(14)
O1^{1}–Co1–O3^{1}	100.04(4)	O4^{2}–Co2–O6^{2}	96.73(5)	O1–Co1–O2	82.67(17)
O1^{1}–Co1– O3^{1}	90.21(4)	O4–Co2–O6^{2}	84.88(5)	O1–Co1–O3	98.51(11)
O1^{1}–Co1–O2	91.43(4)	O4–Co2–O5	105.34(5)	O1–Co1–O4	93.46(11)
O1–Co1–O2	101.26(4)	O4^{2}–Co2–O5	95.23(5)	O1–Co1–N1	163.84(13)
O1–Co1–N2^{1}	165.11(5)	O4–Co2–N5	89.54(5)	O1–Co1–N2	89.13(17)
O1^{1}–Co1–N2^{1}	88.74(5)	O4^{2}–Co2–N5	167.41(5)	O4–Co1–O3	162.23(15)
O1–Co1–N1	87.66(5)	O4–Co2–N6^{2}	159.88(5)	O4–Co1–N1	76.54(16)
O1^{1}–Co1–N1	163.39(5)	O4^{2}–Co2–N6^{2}	87.79(5)	O4–Co1–N2	89.33(16)
O2–Co1–O31	164.74(5)	O6^{2}–Co2–N5	92.35(5)	N1–Co1–O3	94.32(15)
N2^{1}–Co1–O3^{1}	79.13(4)	O6^{2}–Co2–N6^{2}	78.69(5)	N2–Co1–O3	77.82(14)
N2^{1}–Co1–O2	91.18(5)	O5–Co2–O6^{2}	165.18(5)	N2–Co1–N1	103.21(17)
N2^{1}–Co1–N1	103.23(5)	O5–Co2–N5	77.29(5)	Co1^{1}–O1–Co1	97.8(2)
N1–Co1–O3^{1}	93.58(5)	O5–Co2–N6^{2}	93.09(5)	Co1^{1}–O2–Co1	96.9(2)
N1–Co1–O2	77.05(5)	N5–Co2–N6^{2}	102.57(6)		
Co1–O1–Co1^{1}	97.13(5)	Co2–O4–Co2^{2}	97.37(5)		

1′				**2′**			
Co1–O2	2.032(2)	Co2–O2	2.041(3)	Co1–O1	2.0247(19)	Co2–O4^{2}	2.0534(17)
Co1–O6	2.112(2)	Co2–O1	2.032(2)	Co1–O1^{1}	2.0488(17)	Co2–O4	2.0554(18)
Co1–O1	2.039(2)	Co2–O4	2.123(4)	Co1–O2	2.1553(18)	Co2–O5	2.1578(18)
Co1–O3	2.125(3)	Co2–O5	2.091(4)	Co1–O3	2.106(2)	Co2–O6^{2}	2.099(2)
Co1–N4	2.130(3)	Co2–N1	2.130(4)	Co1–N1	2.154(2)	Co2–N5	2.152(2)
Co1–N3	2.138(3)	Co2–N2	2.131(4)	Co1–N2	2.128(2)	Co2–N7^{2}	2.150(2)
O2–Co1–O6	89.26(9)	O2–Co2–O4	96.48(14)	O1–Co1–O1^{1}	82.48(8)	O4^{2}–Co2–O4	83.17(7)
O2–Co1–O1	83.69(10)	O2–Co2–O5	89.11(13)	O1–Co1–O2	87.91(7)	O4–Co2–O5	89.65(7)
O2–Co1–O3	98.63(12)	O2–Co2–N1	166.43(13)	O1^{1}–Co1–O2	101.20(7)	O4^{2}–Co2–O5	96.68(7)
O2–Co1–N4	165.77(11)	O2–Co2–N2	85.19(14)	O1–Co1–O3	101.41(9)	O4^{2}–Co2–O6^{2}	89.15(8)
O2–Co1–N3	85.66(12)	O1–Co2–O2	83.66(10)	O1^{1}–Co1–O3	89.41(8)	O4–Co2–O6^{2}	99.15(8)
O6–Co1–O3	165.95(12)	O1–Co2–O4	88.89(12)	O1^{1}–Co1–N1	161.15(9)	O4–Co2–N5	162.79(8)
O6–Co1–N4	79.30(9)	O1–Co2–O5	101.69(14)	O1–Co1–N1	87.14(8)	O4^{2}–Co2–N5	88.24(8)
O6–Co1–N3	92.40(10)	O1–Co2–N1	91.47(13)	O1^{1}–Co1–N2	90.96(8)	O4–Co2–N7^{2}	89.39(8)
O1–Co1–O6	103.38(10)	O1–Co2–N2	160.74(17)	O1–Co1–N2	163.85(8)	O4^{2}–Co2–N7^{2}	165.33(9)
O1–Co1–O3	89.11(12)	O4–Co2–N1	96.08(16)	O3–Co1–O2	166.78(8)	O6^{2}–Co2–O5	169.98(8)
O1–Co1–N4	90.70(10)	O4–Co2–N2	76.83(16)	O3–Co1–N1	77.24(8)	O6^{2}–Co2–N5	95.59(9)
O1–Co1–N3	160.79(12)	O5–Co2–O4	168.55(15)	O3–Co1–N2	93.24(9)	O6^{2}–Co2–N7^{2}	79.54(8)
O3–Co1–N4	94.33(12)	O5–Co2–N1	79.45(15)	N1–Co1–O2	94.06(8)	N5–Co2–O5	76.53(8)
O3–Co1–N3	76.73(11)	O5–Co2–N2	93.77(18)	N2–Co1–O2	78.86(8)	N7^{2}–Co2–O5	95.90(8)
N4–Co1–N3	103.10(12)	N1–Co2–N2	102.70(17)	N2–Co1–N1	102.88(9)	N7^{2}–Co2–N5	102.04(9)
Co1–O2–Co2	95.80(10)	Co2–O1–Co1	95.89(10)	Co1–O1–Co1^{1}	97.50(8)	Co2^{2}–O4–Co2	95.96(7)

Table S4. Distortion parameters analysis data for complexes **1**, **2**, **1′**, and **2′** by OctaDist-2.6.1 software.

Complex	Temp	Ion	Σ/deg[a]	Θ/deg[b]
1	100.03 K	Co1	75.5018	275.0333
		Co2	75.5008	275.0300
2	100.15 K	Co1	81.0936	285.6360
1′	100.15 K	Co1	78.6956	284.8047
		Co2	79.0368	264.3919
2′	100.15 K	Co1	80.7250	286.7659
		Co2	73.6935	252.8629

[a] The sum of the deviation of 12 unique *cis* ligand-metal-ligand angles from 90°. [b] The sum of the deviation of 24 unique torsional angles between the ligand atoms on opposite triangular faces of the octahedron viewed along the *pseudo*-threefold axis from 60°.

Table S5. CShM analysis data for complexes **1**, **2**, **1′**, and **2′**. The asymmetric unit of **1** and **2′** contains two crystallographically independent halves of the dinuclear cations.

Complex	Temp	Ion	Structure				
			HP-6	**PPY-6**	**OC-6**	**TPR-6**	**JPPY-6**
1	100.03 K	Co1	32.918	22.143	1.962	8.839	25.681
		Co2	31.953	22.243	2.040	8.877	25.740
2	100.15 K	Co1	32.398	21.438	2.141	8.637	24.972
1′	100.15 K	Co1	33.166	22.334	1.983	8.798	25.925
		Co2	33.037	22.643	1.782	9.571	26.347
2′	100.15 K	Co1	33.537	21.786	2.065	8.722	25.499
		Co2	33.351	23.107	1.651	10.053	26.552

Table S6. Crystallographic Geometric Parameters of Co(II) complexes. The asymmetric unit of **1** and **2′** contains two crystallographically independent halves of the dinuclear cations.

	Co···Co (Å)	Ph1 and Ph2(°)	Ph1/2 and Co_2O_2 (°)	Co–O–Co (°)
1	3.042	0	8.931	97.135
	3.067	0	4.024	97.367
2	3.083	14.266	9.091	97.770
			5.175	96.888
1′	3.022	142.791	166.076	95.808
			23.285	95.877
2′	3.063	25.514	12.757	97.497
	3.052	23.828	11.914	95.952

Table S7. Magnetic coupling constants of **1** and **2** obtained from broken-symmetry calculations (B3LYP/ZORA-def2-TZVP, units: cm^{-1}).

	J (1)	J (2)	J (3)
1	–0.26	–0.20	–0.26
2	–1.39	–1.04	–1.39

Table S8. The Peak potential separation (ΔE) of **1** and **2** increases progressively with scan rate ($v^{1/2}$).

	$v^{1/2}$ (mV s^{-1})	ΔE (mV)
1	50	159
	100	177
	200	222
	300	262
2	50	214
	100	234
	150	276
	200	287

Table S9. Peak Potentials (a = anodic, c = cathodic) at a scan rate of 100 mV s^{-1} for **1** and **2**, determined by Open-Circuit Potential (OCP) and Cyclic Voltammetry (CV) measurements in HEPES buffer (25 °C).

	OCP (mV vs NHE)	$E_{p,a}$ (mV vs NHE)	$E_{p,c}$ (mV vs NHE)	$E_{1/2}$ (mV)
1	429	811	624	718
2	559	720	446	583

Table S10. Single point energy and solution Gibbs free energy (298.15 K/25 °C) of isomeric complexes **1** (*syn*) and **2** (*anti*) in the boat and chair configurations (units: Hartree).

	1-boat	**1-chair**	**2-boat**	**2-chair**
E_{el} PBE0-SMD	-4900.178749	-4900.176908	-4900.180264	-4900.178585
ZPE	0.78856827	0.78814857	0.78871890	0.78902311
U	-4899.3435144	-4899.3420567	-4899.3449430	-4899.3430879
H	-4899.3425702	-4899.3411125	-4899.3439988	-4899.3421437
G	-4899.4613567	-4899.4600402	-4899.4624973	-4899.4604603
G_n	0.71739287	0.71686698	0.71776780	0.71812448
ΔG (kcal/mol)	0.72	1.54	0	1.28

Table S11. Relaxation times (T_i) and relaxation rates (r_i) of H_2O in HEPES buffer containing various concentrations of **1** or **2** and measured at 37 °C.

Conc. (mM)	**1** (pH 7.59)		**2** (pH 7.44)	
	T_1 (ms)	T_2 (ms)	T_1 (ms)	T_2 (ms)
10	1633	767.848	1397	711.596
8	1946	956.374	1447	744.572
6	2148	1123.848	1747	882.388
4	2392	1390.568	2589	1189.602
2	2768	1921.97	3316	1564.709

	1	**2**
R_1 (mM^{-1} s^{-1})	0.0299	0.05667
R_2 (mM^{-1} s^{-1})	0.09453	0.10174

Table S12. Comparison of % CEST of the Co(II) analogues and Ln-paraCEST.

Complexes	**Ligand**	**Chemical Shift (ppm)**	**CEST (%)**	**Conc. (mM)**	***N*[a]**	***m*[b]**	**Conditions**
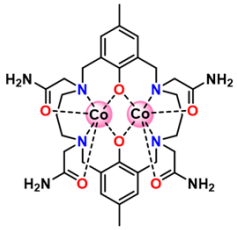	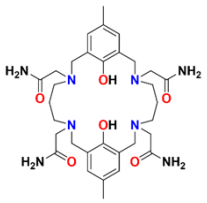	78.5/73	51/52	10	8	4	9.4 T NMR, B_1 = 20 μT×4 s, 37 °C, pH = 7.46
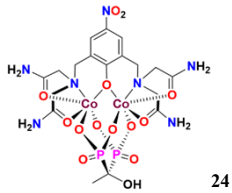 **24**	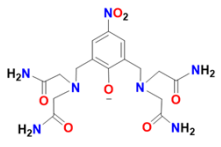	106	27	12.8	8	4	9.4 T NMR, B_1 = 24 μT×6 s, 37 °C, pH = 8.14
 **25**	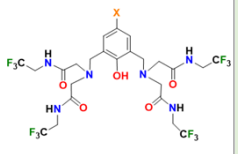	79	<25%	9	8	4	9.4 T NMR, B_1 = 21 μT×4 s, 37 °C, pH = 7.80

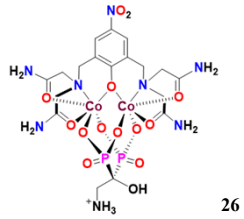 26	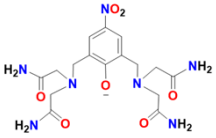	48	42	8	8	4	11.7 T NMR, B_1 = 22 μT×2 s, 37 °C, pH = 7.01
Co-CCRM[27]	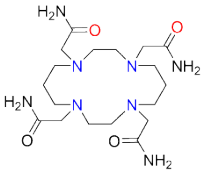	45	38±1%	10	8	2	11.7 T NMR, B_1 = 29 μT, 37 °C, pH = 7.4
Co-TCMT[28 29]	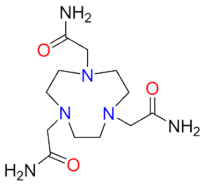	32	33	10	6	3	11.7 T NMR, B_1 = 24 μT×2 s, 37 °C, pH = 7.4
Co-NOPE[30 31]	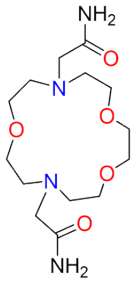	59	38	10	4	2	11.7 T NMR, B_1 = 24 μT×2 s, 37 °C, pH = 7.4
Co-TCMC[32]	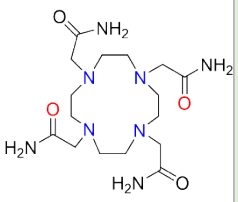	45	21	10	8	4	11.7 T NMR, B_1 = 24 μT×2 s, 37 °C, pH = 7.5
Co-HINO[33]	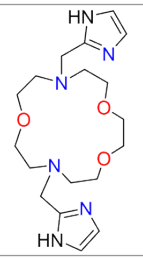	32	24	8	2	1	11.7 T NMR, B_1 = 24 μT×4 s, 37 °C, pH = 7.0
Co-TPTA[34]	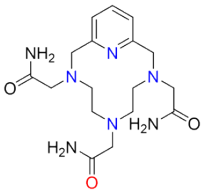	57	30	10	4	2	9.4 T NMR, B_1 = 25 μT×2 s, 37 °C, pH = 7.4

Co-CYNO[28]	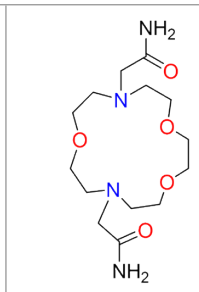	59	38	10	4	2	11.7 T NMR, B_1 = 24 μT×2 s, 37 °C, pH = 7.4
Co(TPT)[35]	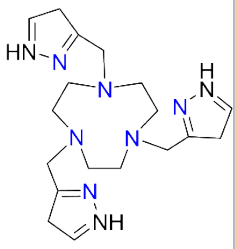	135	21	8	3	3	11.7 T NMR, B_1 = 24 μT×3 s, 37 °C, pH = 7.0
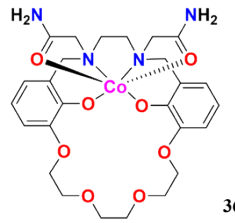 **36**	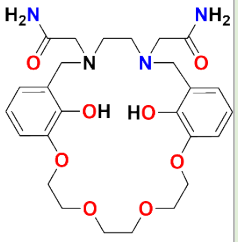	80	8.5	5	4	2	11.7 T NMR, B_1 = 21 μT×3 s, 37 °C, pH = 7.4
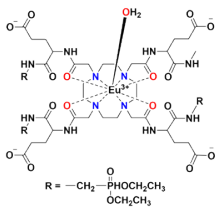 **37**	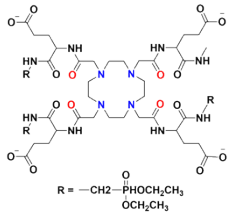	40	~65%	20	8	4	9.4 T NMR, B_1 = 20 μT×5 s, 37 °C, pH = 7.0
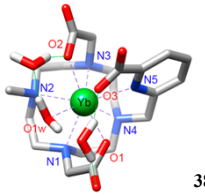 **38**, *c*	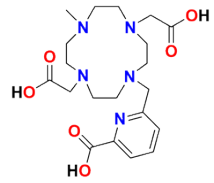	176	33	15	2	2	7.05 T, B_1 = 30 μT×10 s, 25 °C, pH = 7.0
 **39**	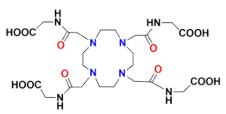	−16	70	30	4	4	7.05 T, B_1 = 25 μT×4 s, 39 °C, pH = 8.1
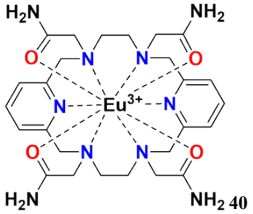 **40**	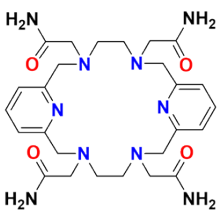	14	5	~25	8	4	7.05 T, B_1 = 5 μT×5 s, 37 °C, pH = 7.4

[a] Total number of exchangeable amide protons in the paraCEST agent.

[b] Number of magnetically equivalent amide protons that give rise to a CEST peak.

[c] Optimized geometries obtained with DFT calculations

Table S13. Co–H (from exchangeable –NH_2) distances of Co(II) complexes.

	1 (Å)		**2** (Å)		**1'** (Å)		**2′** (Å)	
$d_{Co\text{-}H}$	Co1-H3a	4.542	Co1-H3b	4.818	Co1-H5a	4.498	Co1-H3a	4.572
	Co1-H3b	4.764	Co1-H3a	4.611	Co1-H5b	4.738	Co1-H3b	4.808
	Co1-H4b	4.784	Co1-H4a	4.538	Co1-H8c	4.473	Co1-H4a	4.496
	Co1-H4a	4.564	Co1-H4b	4.780	Co1-H8d	4.695	Co1-H4b	4.725
	Co2-H7a	4.539			Co2-H7b	4.705	Co2-H8b	4.747
	Co2-H7b	4.781			Co2-H7a	4.504	Co2-H8a	4.511
	Co2-H8d	4.781			Co2-H6a	4.445	Co2-H6a	4.561
	Co2-H8c	4.555			Co2-H6b	4.700	Co2-H6b	4.806

4. Additional Figures

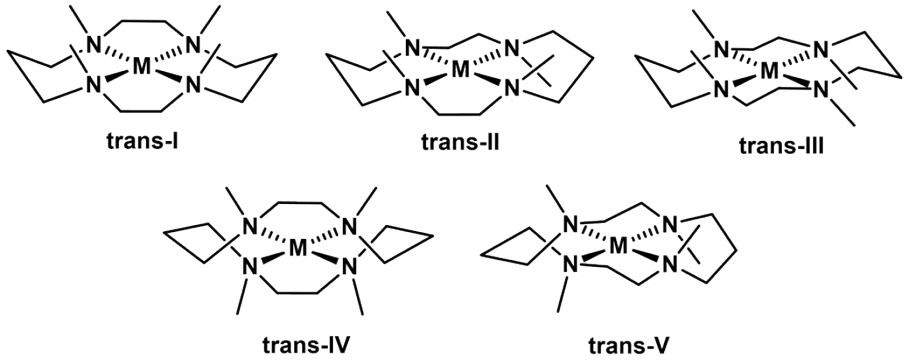

Figure S1. *Trans*-I–V conformers of 1,4,8,11-tetraazacyclotetradecane (cyclam) ligands.

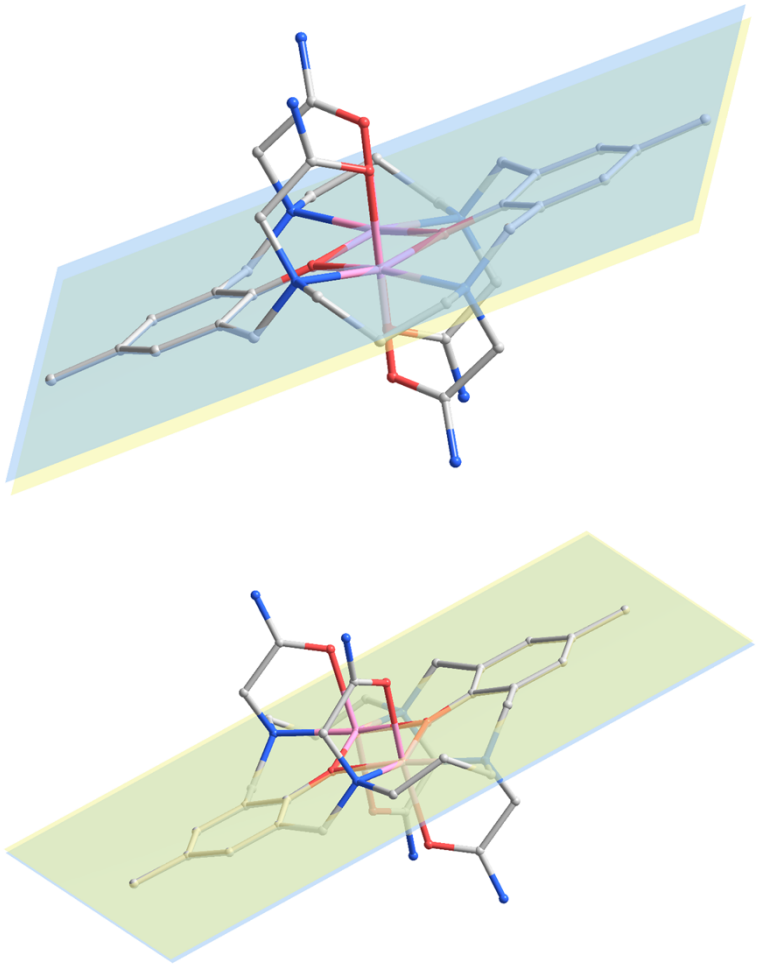

Figure S2. The dihedral angle between the phenolato rings of **1** is 0°, 0°. The asymmetric unit contains two crystallographically independent halves of the dinuclear cations.

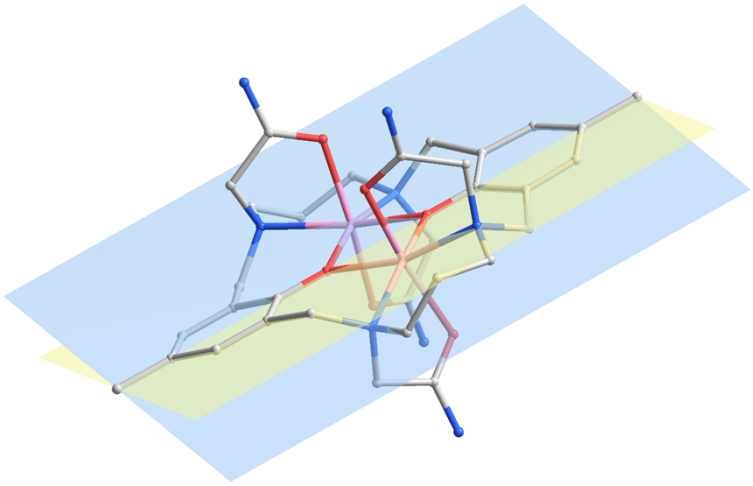

Figure S3. The dihedral angle between the phenolato rings of of **2** is 14.27°.

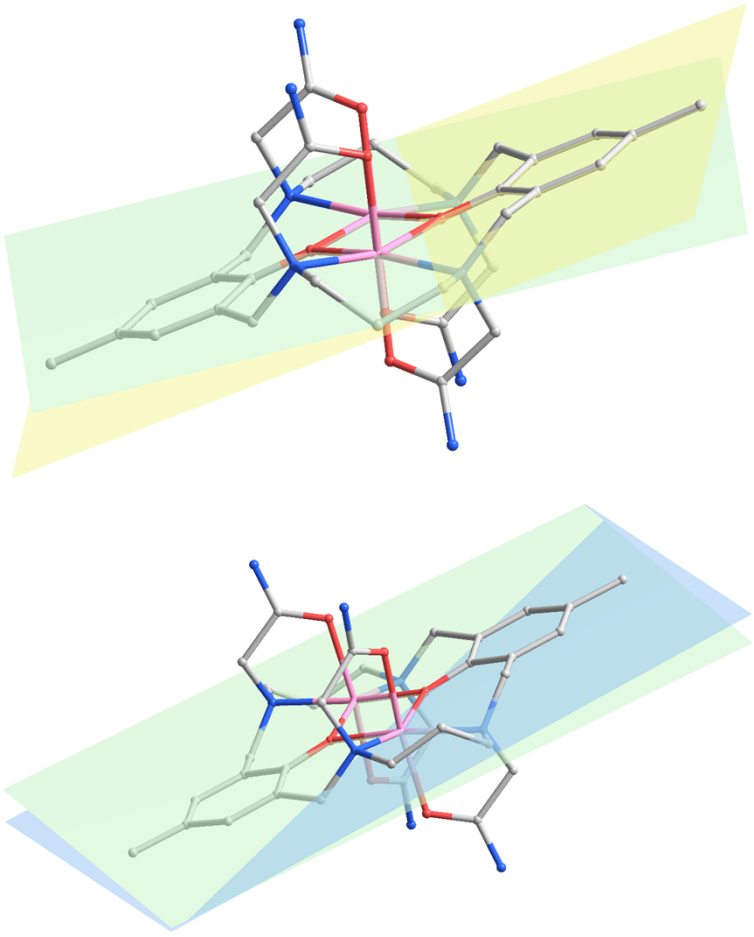

Figure S4. The phenolato-ring and the Co_2O_2 plane of **1** form a dihedral angle of 8.93º, 4.02º. The asymmetric unit contains two crystallographically independent halves of the dinuclear cations.

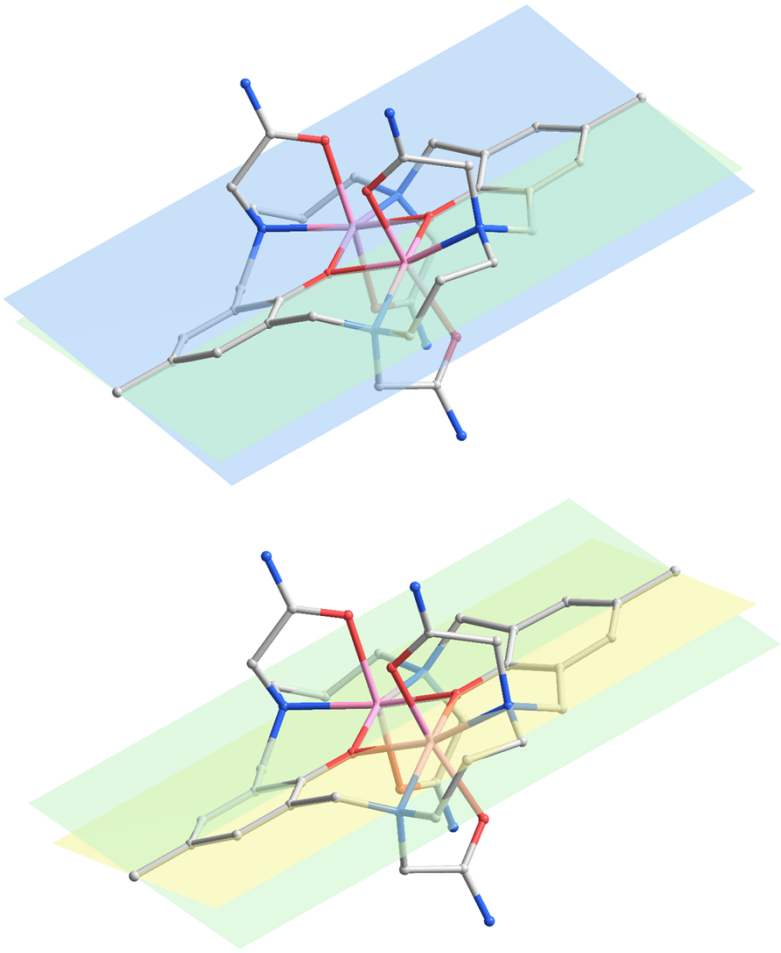

Figure S5. The phenolato-ring and the Co_2O_2 plane of **2** form a dihedral angle of 9.09°, 5.18°.

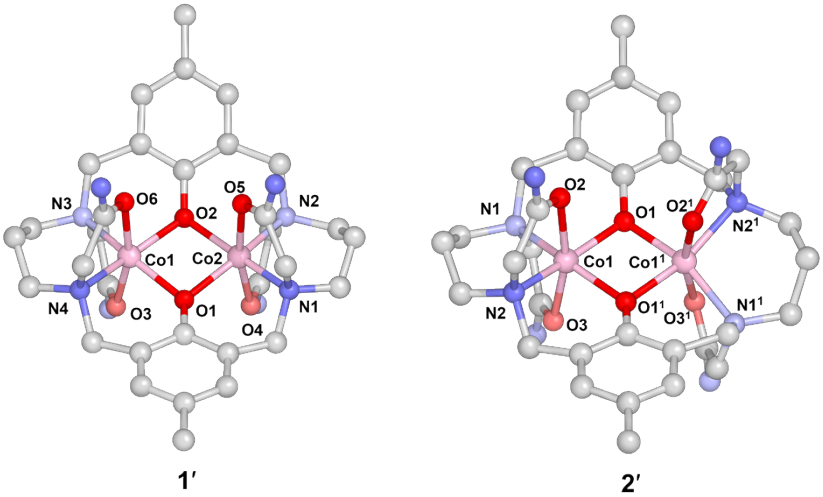

Figure S6. Crystal structures of **1′** and **2′**. Hydrogen atoms, solvent molecules, and counter anions are omitted for clarity. C, gray; N, slate; O, red; Co, pink.

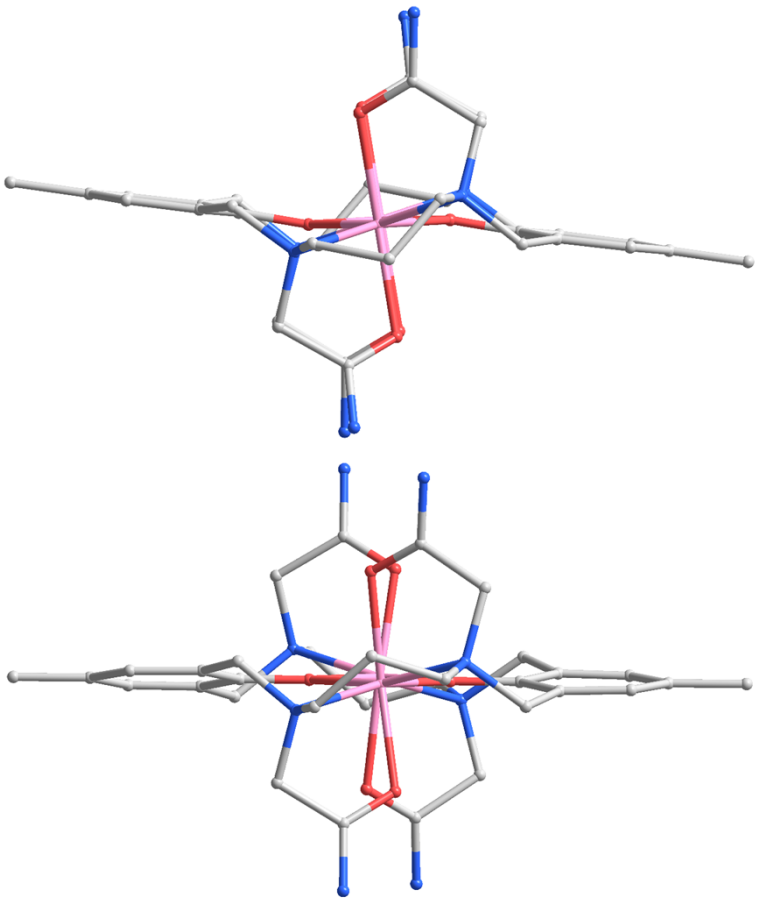

Figure S7. Chair conformation of **1** (top)and **2** (bottom).

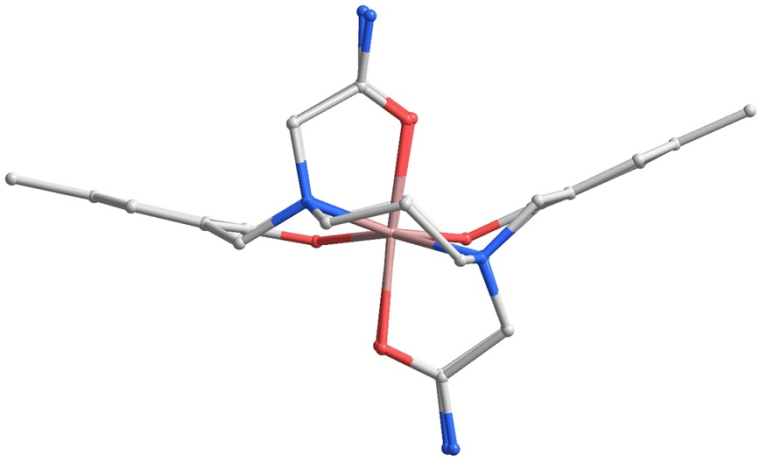

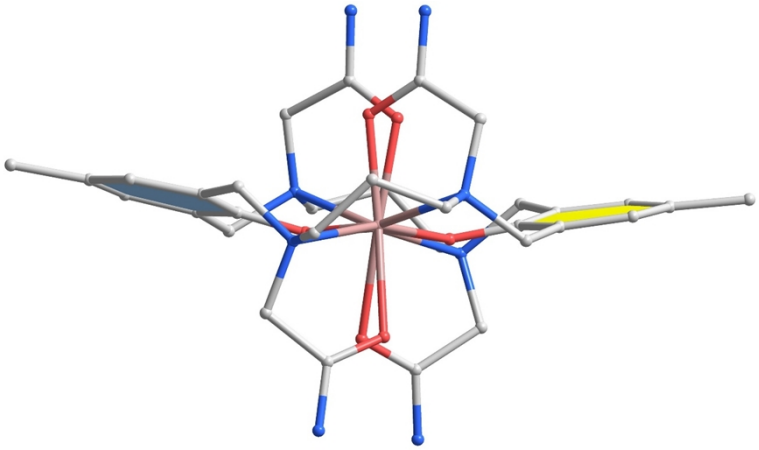

Figure S8. Boat conformation of **1′** (top) and **2′** (bottom).

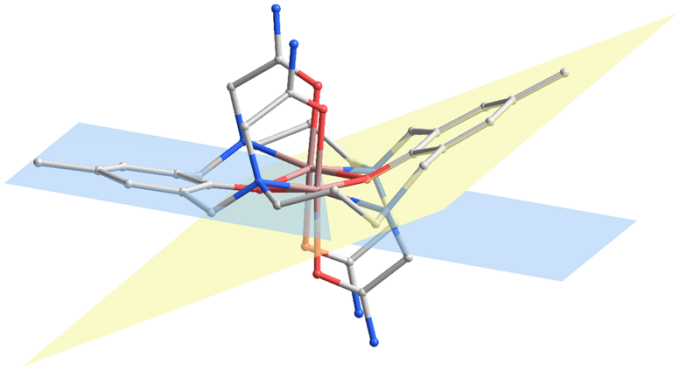

Figure S9. The dihedral angle between the phenolato rings of of **1′** is 143.79°, with the corresponding acute angle being 36.21°.

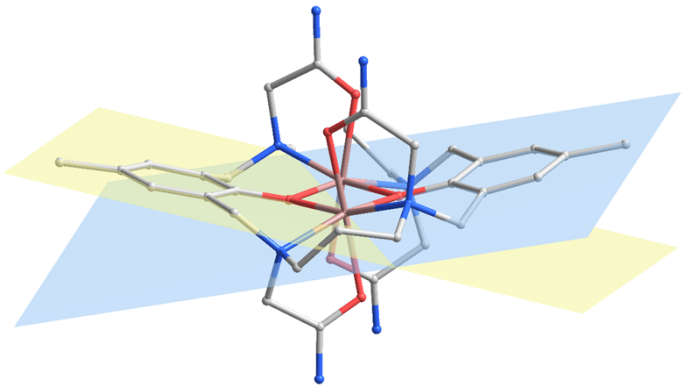

Figure S10. The dihedral angle between the phenolato rings of of **2′** is 25.51°, 23.83°, with the corresponding obtuse angles being 154.49° and 156.17° for the two crystallographically independent dinuclear cations.

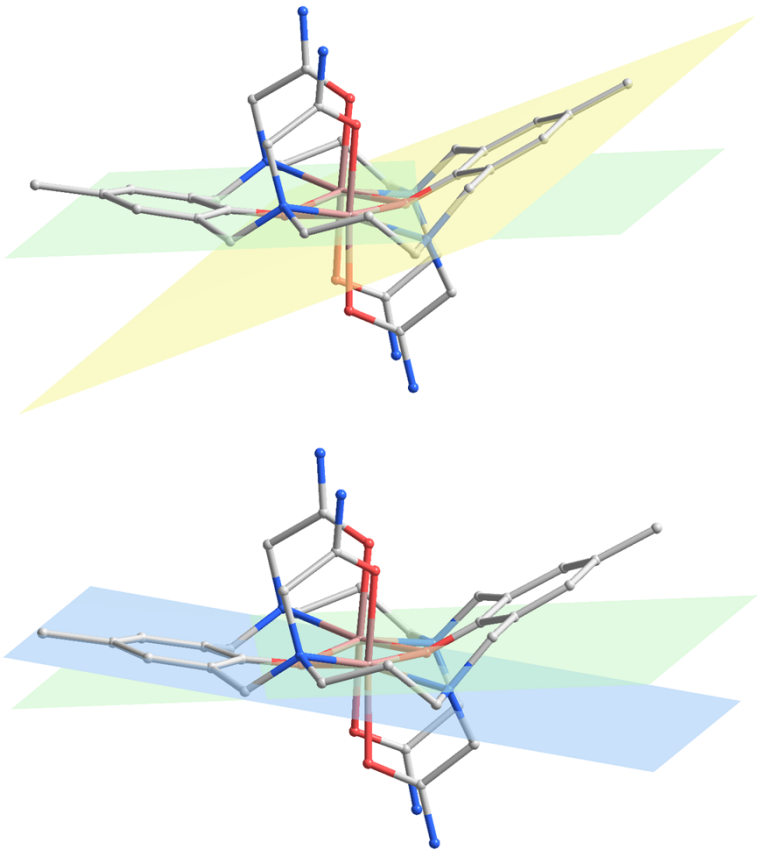

Figure S11. The phenolato-ring and the Co_2O_2 plane of **1'** form a dihedral angle of 156.72°, 166.08°, with the corresponding acute angles being 23.28° and 13.92°.

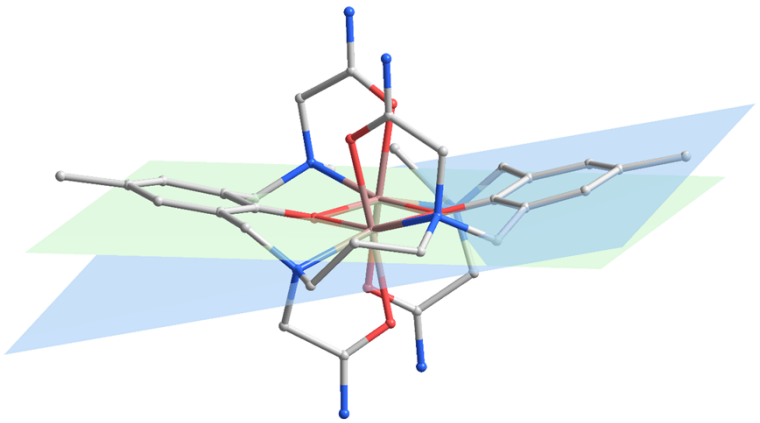

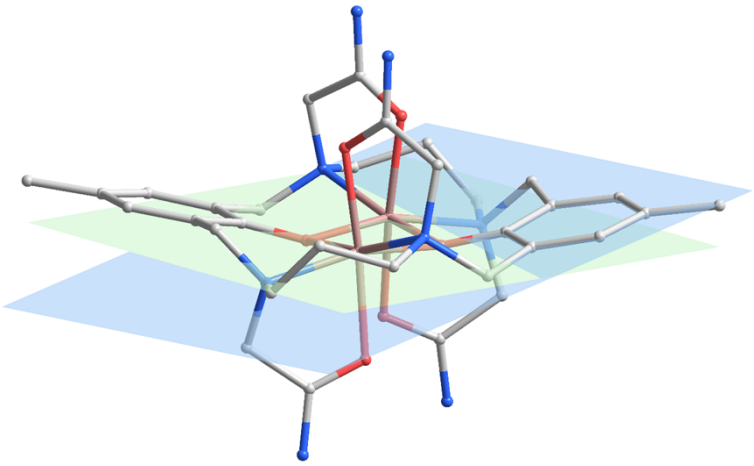

Figure S12. The phenolato-ring and the Co_2O_2 plane of **2′** form a dihedral angle of 11.91°, 12.76°, with the corresponding obtuse angles being 168.09° and 167.24° for the two crystallographically independent dinuclear cations.

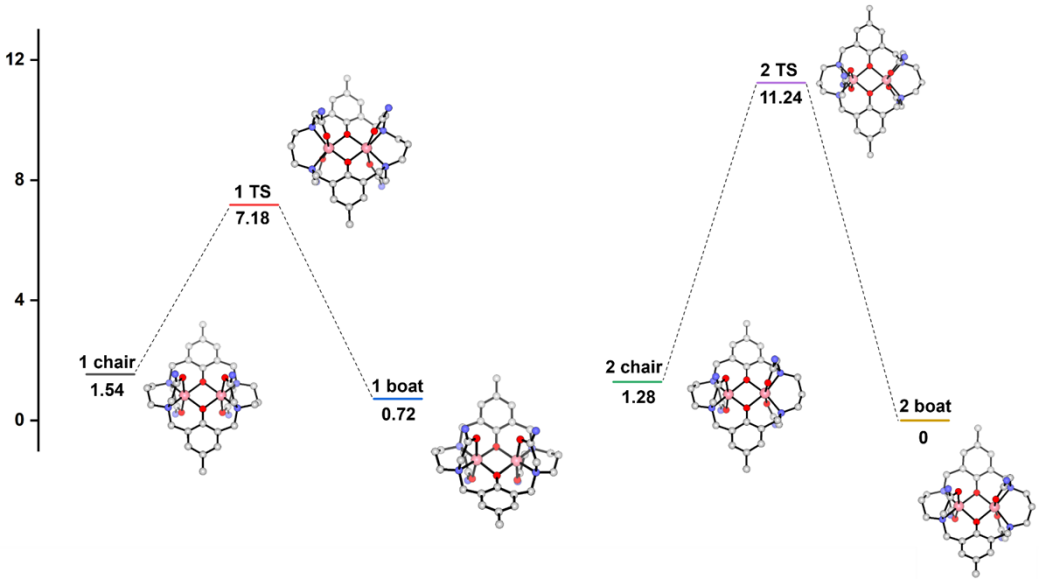

Figure S13. Energy diagram for **1** and **2** (unit: kcal mol^{-1}).

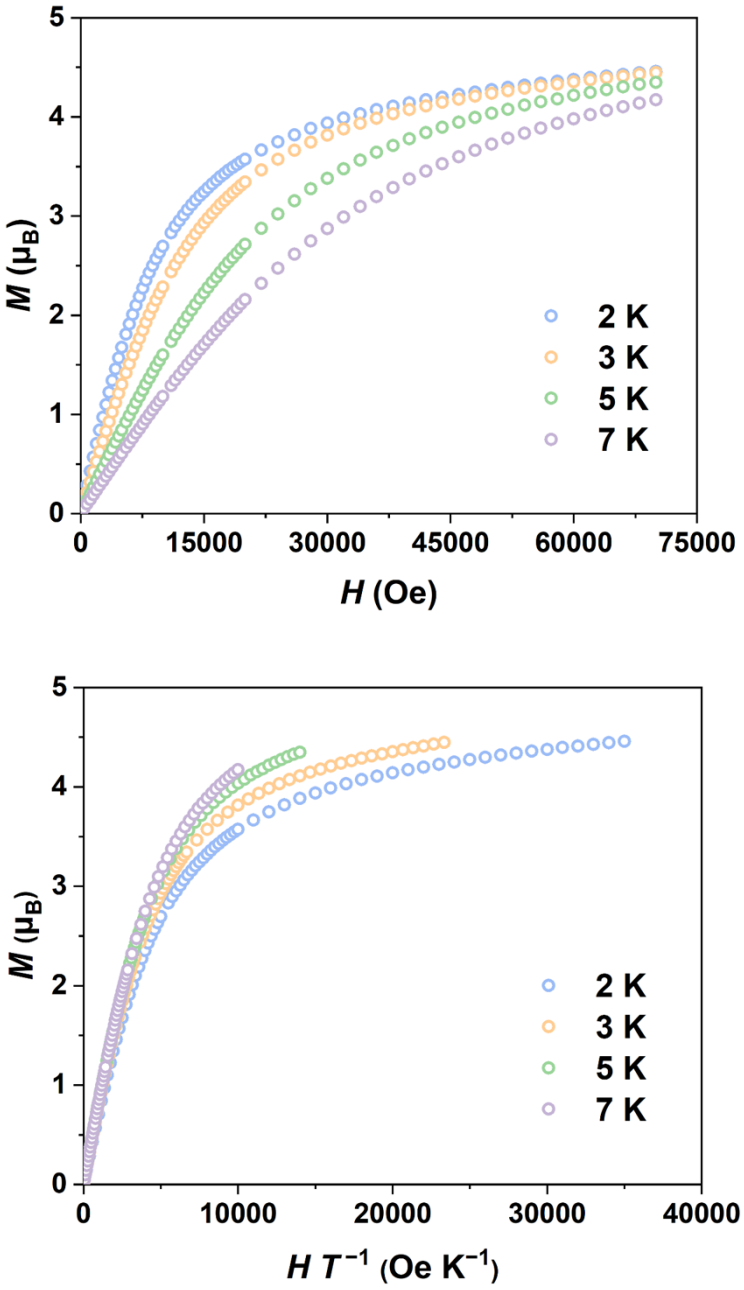

Figure S14. Magnetization and reduced magnetization curves of **1** at the respective temperatures.

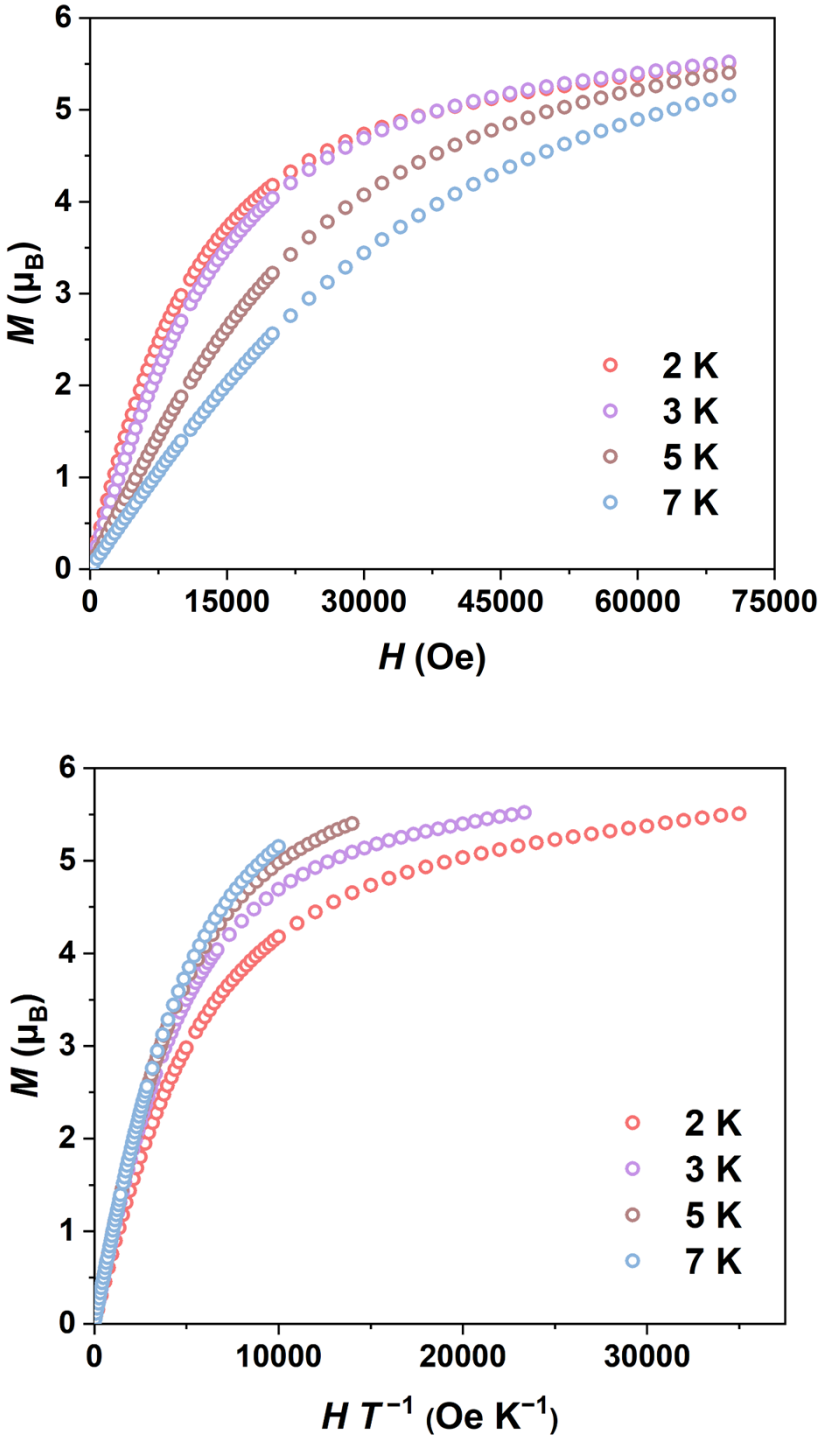

Figure S15. Magnetization and reduced magnetization curves of **2** at the respective temperatures.

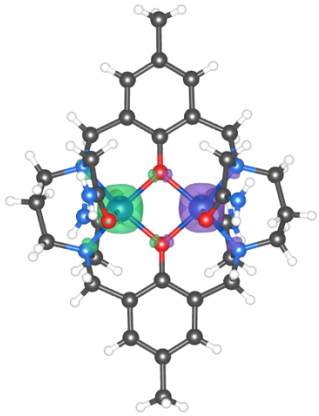	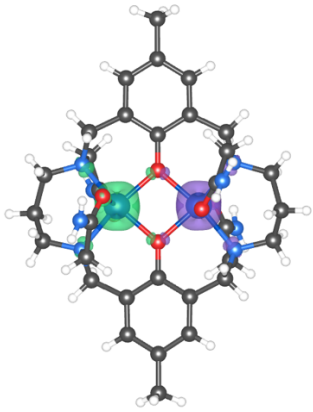
1	**2**

Figure S16. DFT calculated broken-symmetry spin density distribution for **1** and **2** (isovalue: 0.01 a.u.).

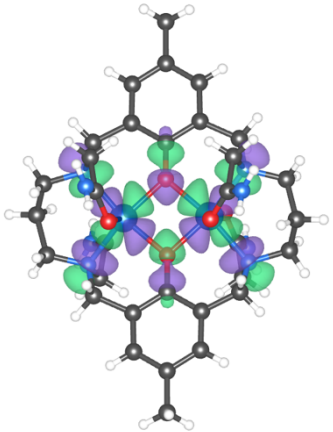	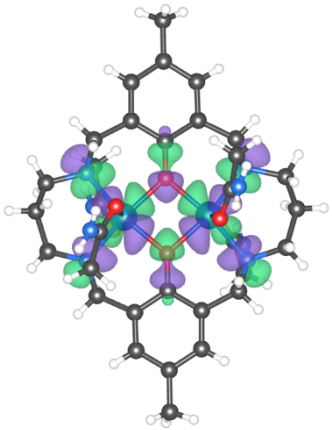
1 ($S_{\alpha\beta} = 0.06$, d_{xy})	**2** ($S_{\alpha\beta} = 0.06$, d_{xy})
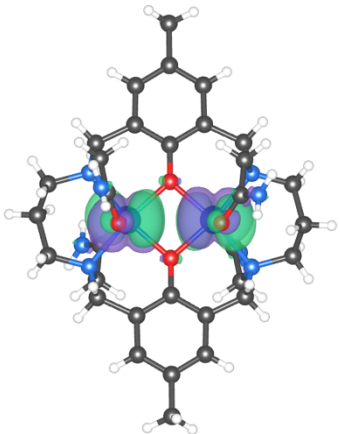	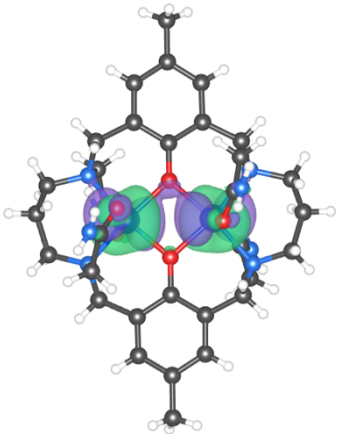
1 ($S_{\alpha\beta} = 0.04$, d_{xz})	**2** ($S_{\alpha\beta} = 0.04$, d_{xz})

Figure S17. Symmetric combinations of the d_π magnetic orbitals of adjacent high-spin Co(II) atoms responsive for antiferromagnetic coupling in **1** and **2** (isovalue: 0.02 a.u.), S_{ab} denotes overlap integral.

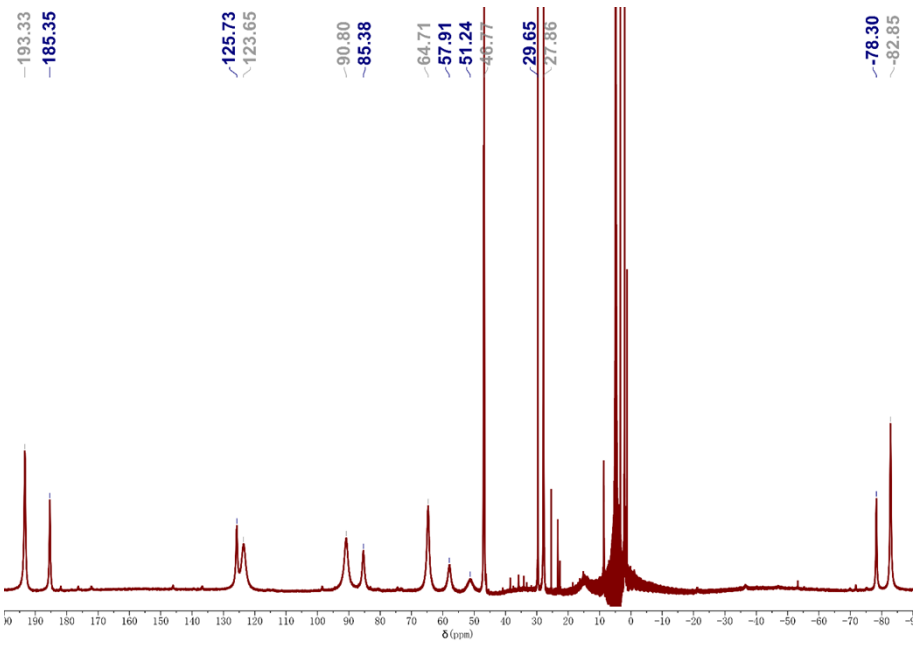

Figure S18. ^{1}H NMR of **1** (grey-labeled peaks) and **2** (blue-labeled peaks) in D_2O, acquired during the single crystal growth process.

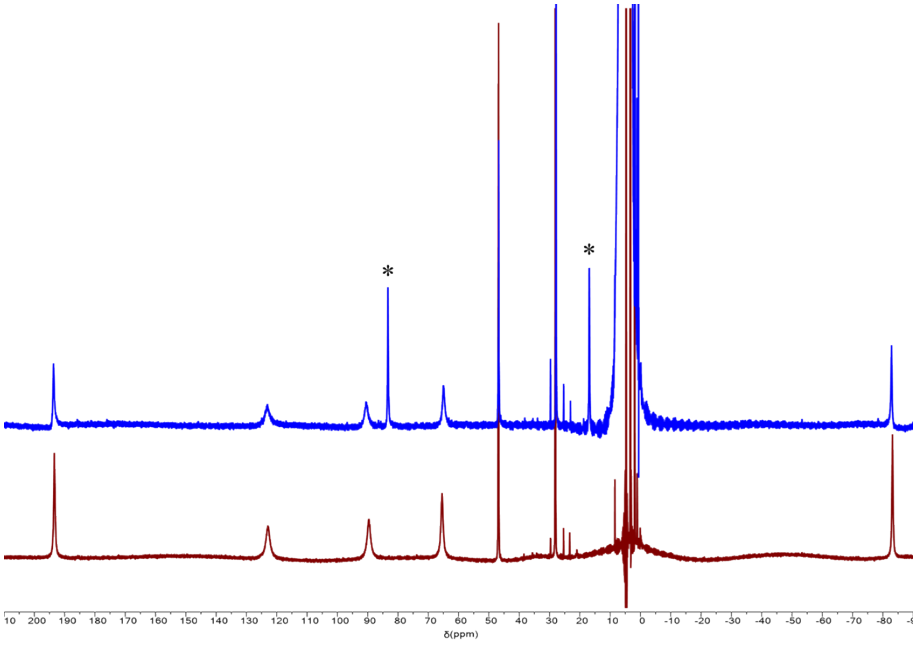

Figure S19. 400 MHz ^{1}H NMR spectrum of **1** in D_2O (red) and HEPES buffer (blue, pH = 6.85) of 50 mM HEPES and 100 mM NaCl.

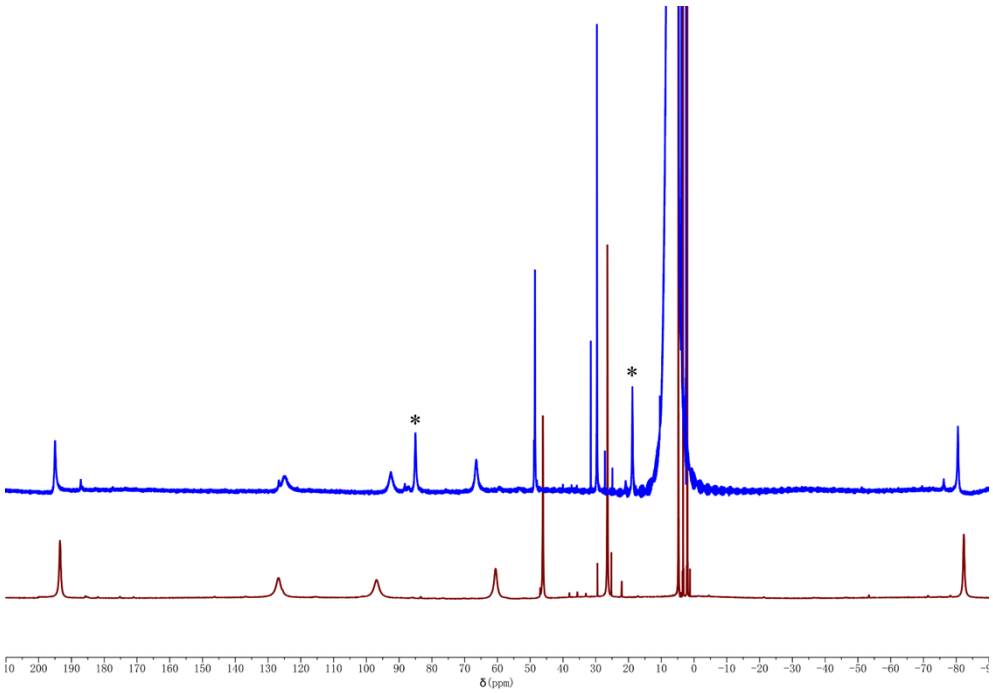

Figure S20. 400 MHz ^{1}H NMR spectrum of **1** in D_2O (red) and HEPES buffer (blue, pH = 7.40) of 50 mM HEPES and 100 mM NaCl.

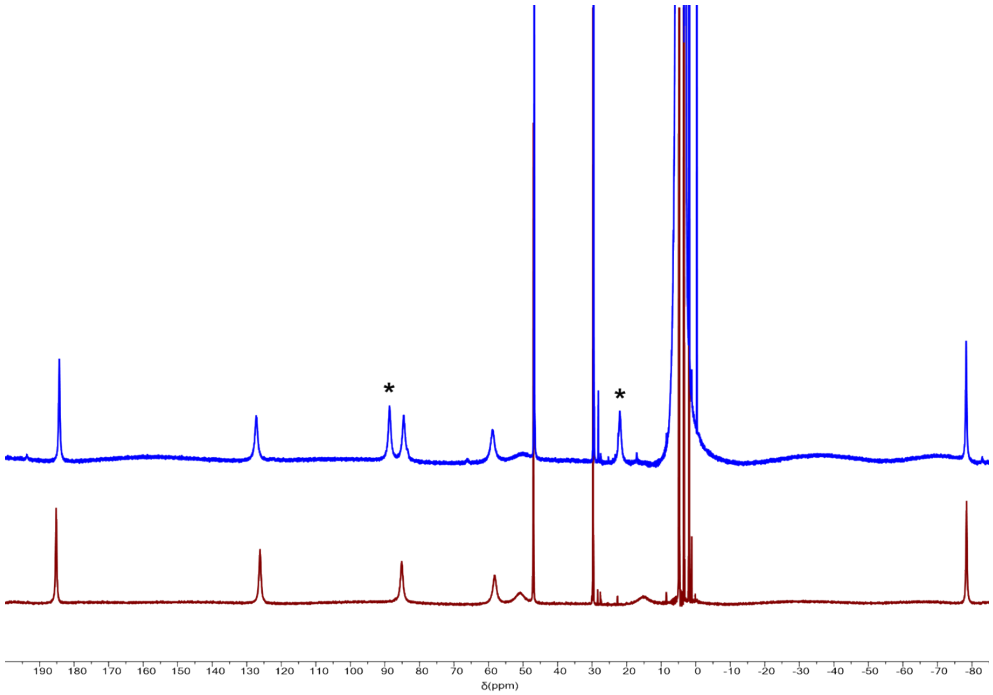

Figure S21. 400 MHz ^{1}H NMR spectrum of **2** in D_2O (red) and HEPES buffer (blue, pH = 7.35) of 50 mM HEPES and 100 mM NaCl.

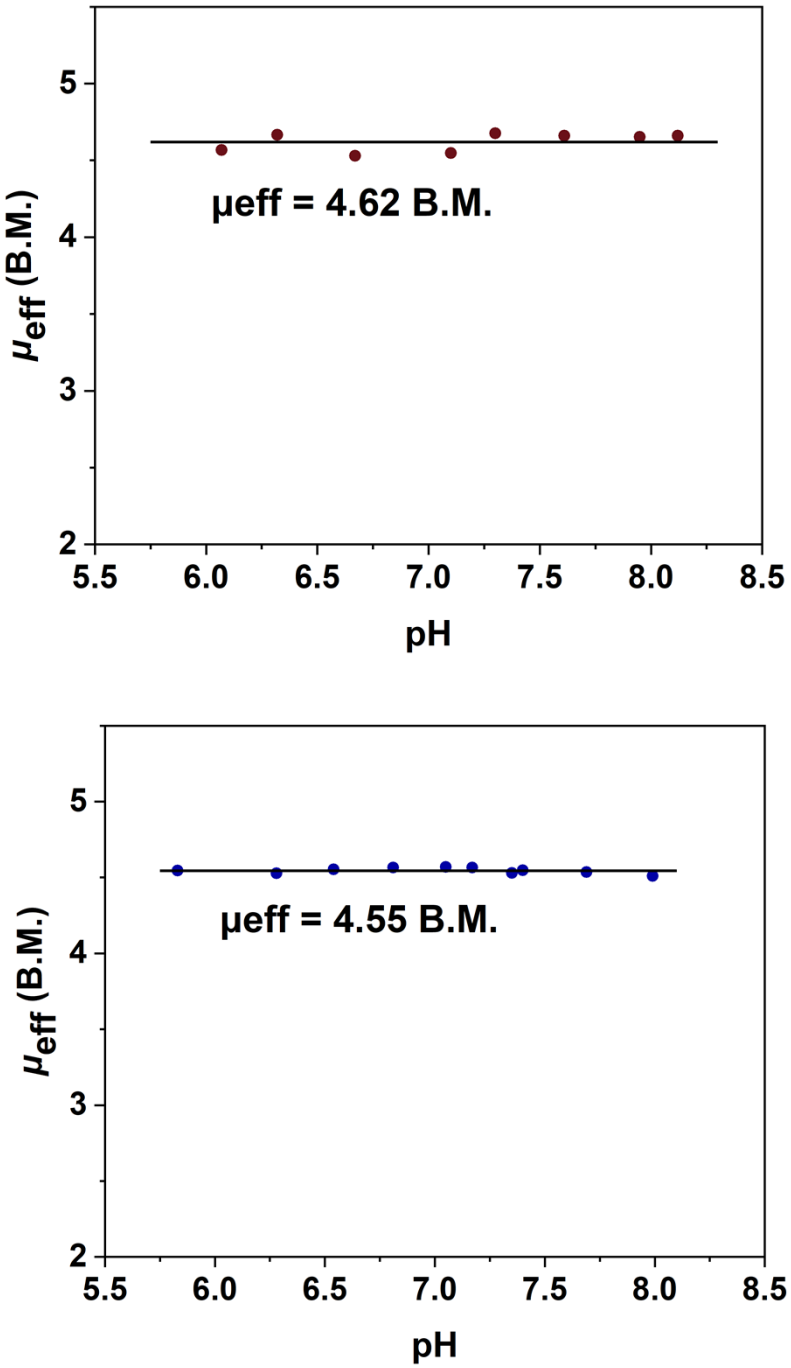

Figure S22. Variable-pH magnetic susceptibility data for **1** (top) and **2** (bottom) in aqueous solutions containing 50 mM HEPES and 100 mM NaCl at 25 °C, obtained using the Evans method.

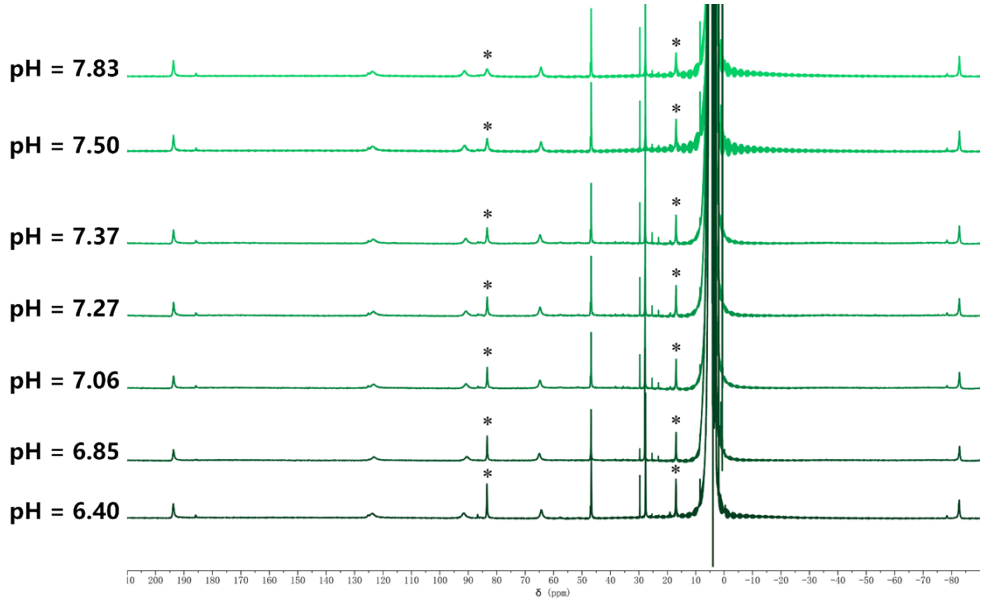

Figure S23. Variable-pH ^{1}H NMR spectra of 10 mM of **1** in aqueous solutions containing 50 mM HEPES and 100 mM NaCl buffered to various pH values, collected at 37 °C and 9.4 T.

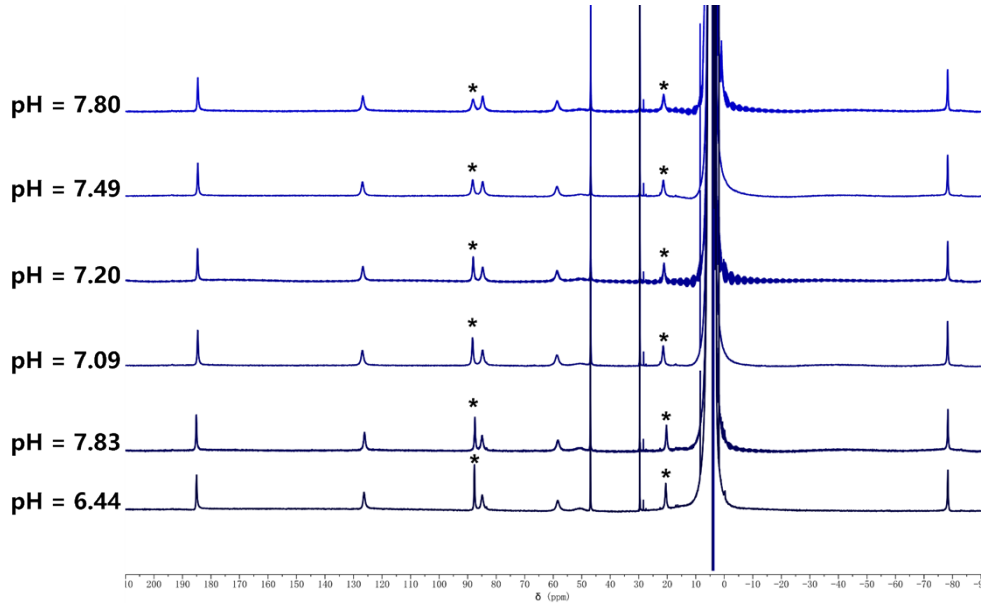

Figure S24. Variable-pH ^{1}H NMR spectra of 10 mM of **2** in aqueous solutions containing 50 mM HEPES and 100 mM NaCl buffered to various pH values, collected at 37 °C and 9.4 T.

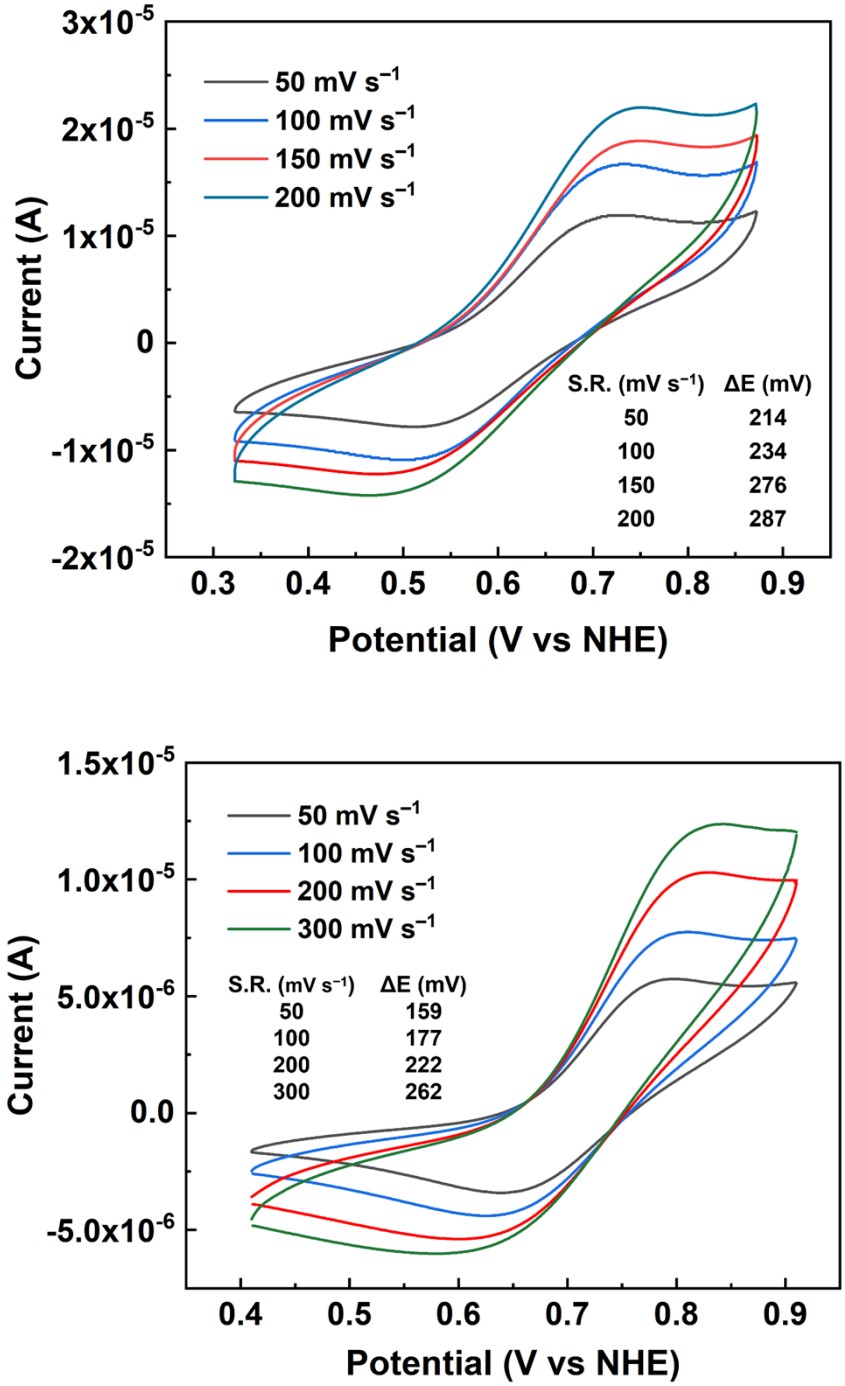

Figure S25. Cyclic voltammogram for 1 mM of **1** and **2** in an aqueous solution containing 50 mM HEPES and 100 mM NaCl buffer (pH 7.4) at 25 °C, with different scan rates.

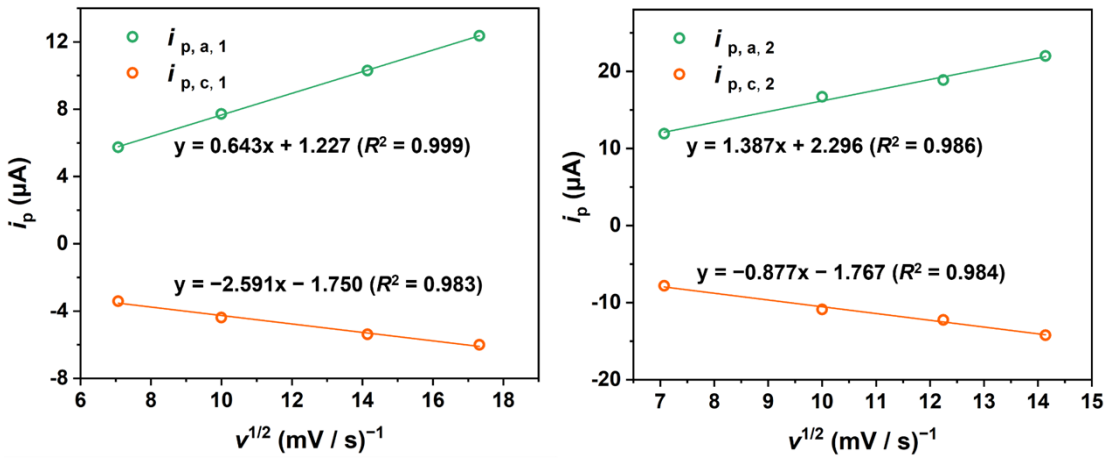

Figure S26. Linear fitting plots of cathodic and anodic peak currents versus the square root of scan rate ($v^{1/2}$).

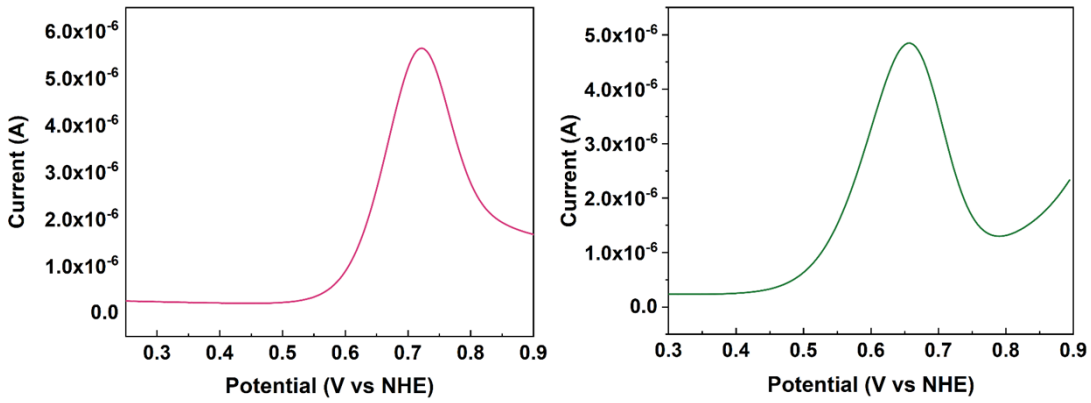

Figure S27. Differential Pulse Voltammetry (DPV) for **1** (red) and **2** (green) in HEPES at 25 °C.

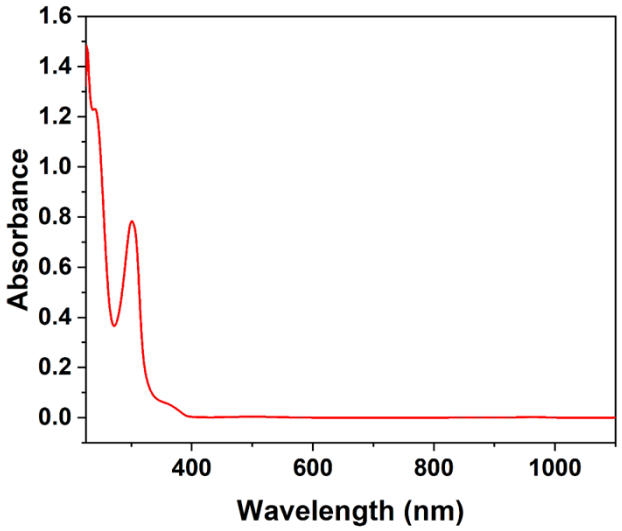

Figure S28. UV–vis spectrum of a solution containing 0.10 mM of **1** in 50 mM HEPES and 100 mM NaCl at pH 7.35. An absorption band at 301 nm (ε = 7250 M^{-1} cm^{-1}) was observed, corresponding to the $n \rightarrow \pi^*$ transition of the phenolate groups.

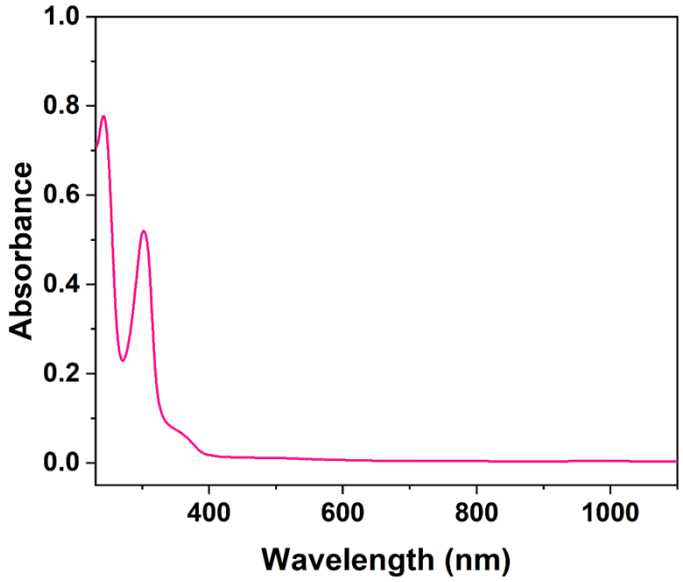

Figure S29. UV–vis spectrum of a solution containing 0.10 mM of **2** in 50 mM HEPES and 100 mM NaCl at pH 7.35. An absorption band at 302 nm ($\varepsilon = 5200\ M^{-1}\ cm^{-1}$) was observed, corresponding to the $n \rightarrow \pi^*$ transition of the phenolate groups.

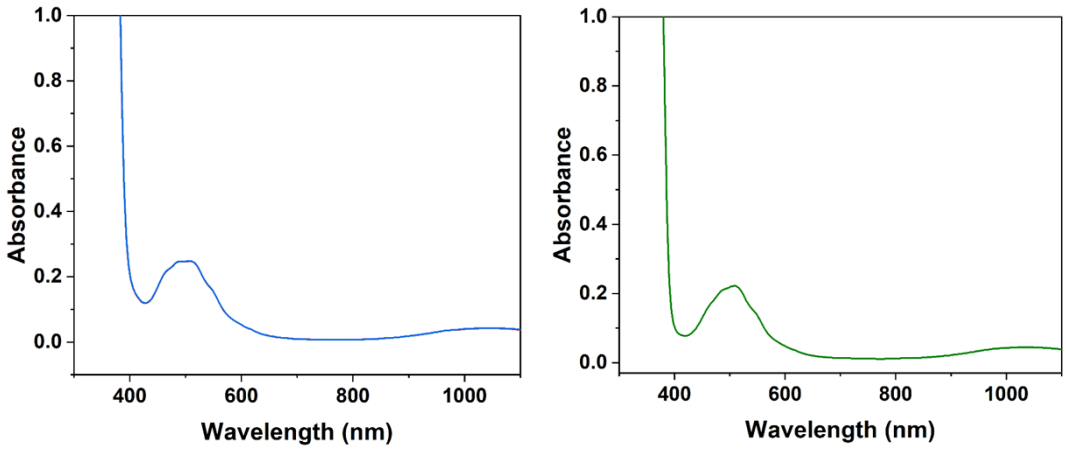

Figure S30. UV–vis spectrum of a solution containing 5 mM of **1** (left) and **2** (right) in 50 mM HEPES and 100 mM NaCl at pH 7.35. An absorption maximum at 506/509 nm is observed for the complex, which is derived from the $^4T_{1g}(F) \rightarrow {}^4T_{1g}(P)$ transition. The shoulder peak results from spin-orbit coupling-induced degeneracy lifting in the excited $^4T_{1g}(P)$ state, with the slight band splitting arising from the complexes' lowered local Oh symmetry[41].

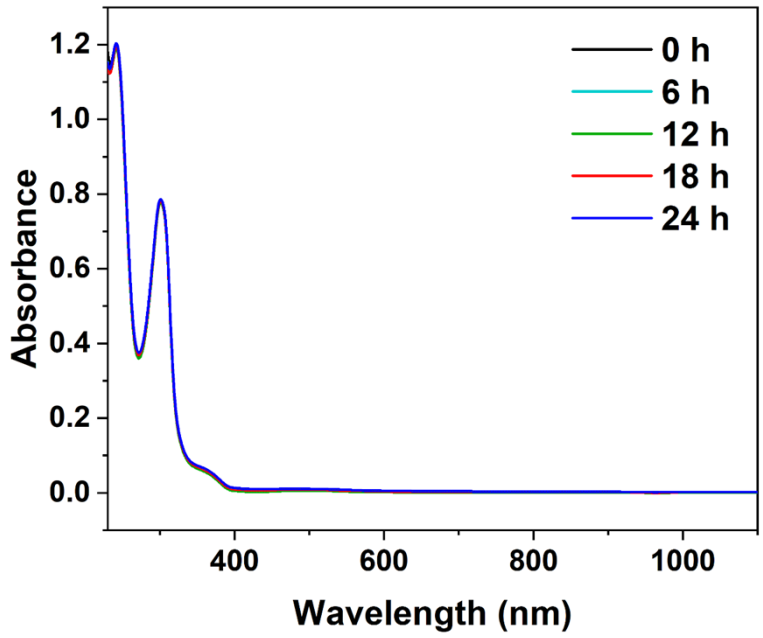

Figure S31. UV–vis spectra of a solution containing 0.10 mM of **1** in 50 mM HEPES and 100 mM NaCl at pH 7.35, the solution was scanned immediately after the addition of 5 mM $CaCl_2$.

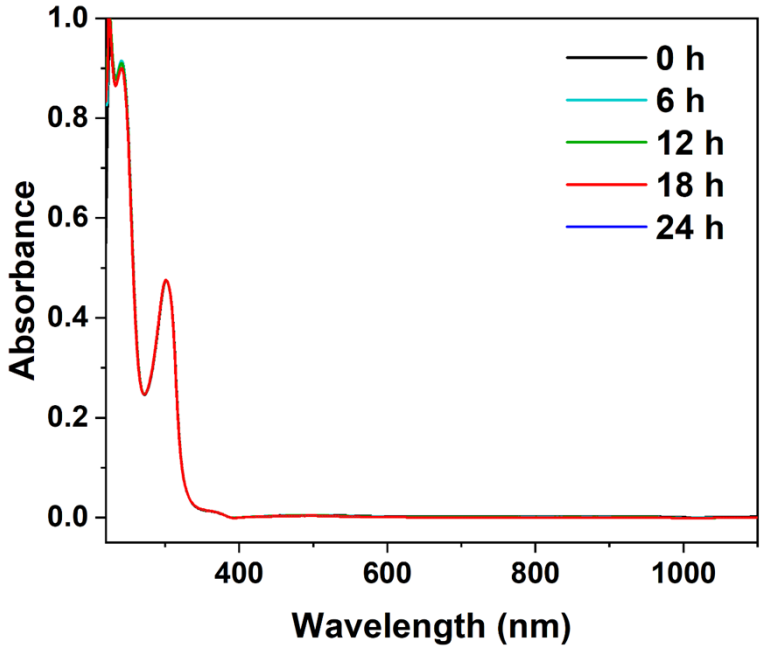

Figure S32. UV–vis spectra of a solution containing 0.10 mM of **2** in 50 mM HEPES and 100 mM NaCl at pH 7.35, the solution was scanned immediately after the addition of 5 mM $CaCl_2$.

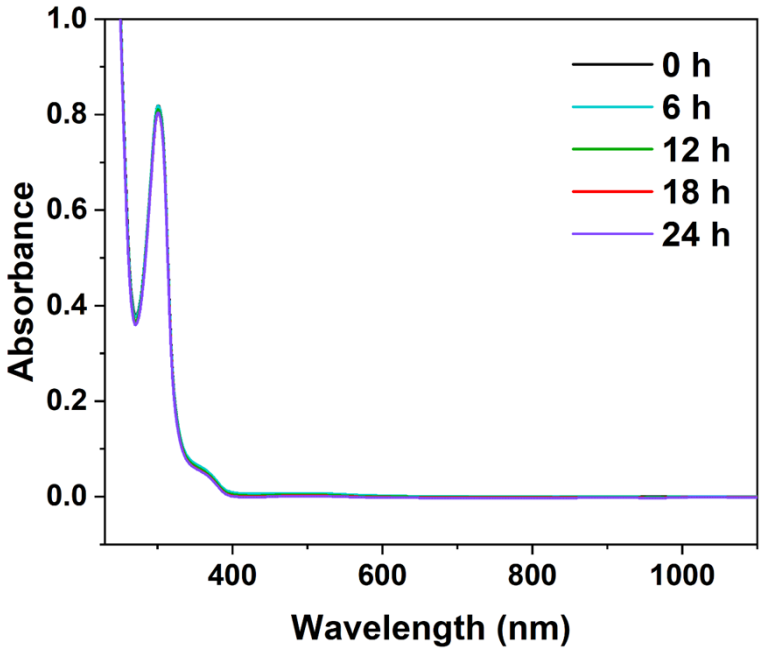

Figure S33. UV–vis spectra of a solution containing 0.10 mM of **1** in 50 mM HEPES and 100 mM NaCl at pH 7.35, the solution was scanned immediately after the addition of 4 mM $ZnCl_2$.

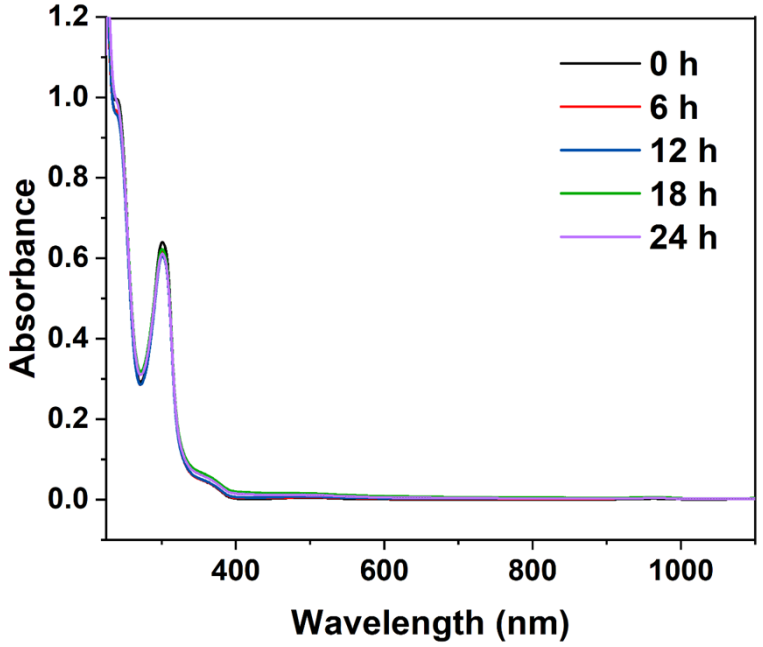

Figure S34. UV–vis spectra of a solution containing 0.10 mM of **2** in 50 mM HEPES and 100 mM NaCl at pH 7.35, the solution was scanned immediately after the addition of 4 mM $ZnCl_2$.

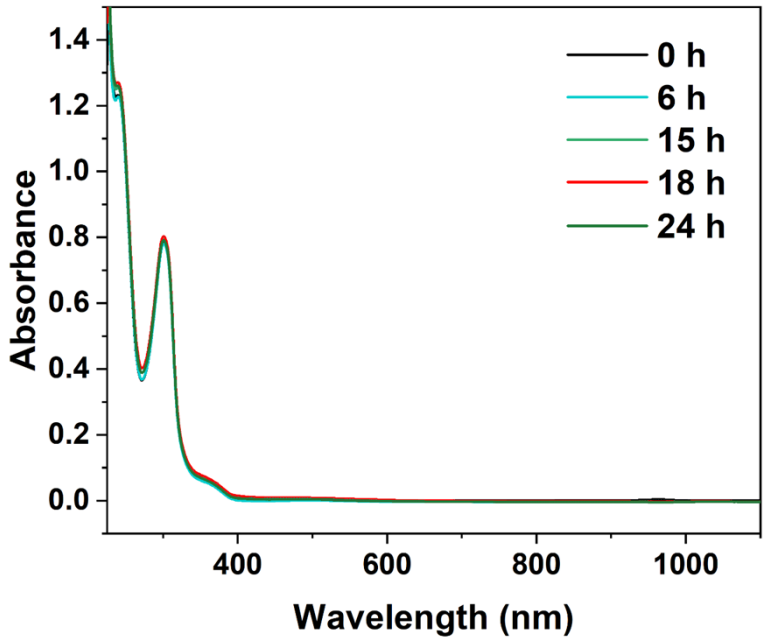

Figure S35. UV–vis spectra of a solution containing 0.10 mM of **1** in 50 mM HEPES and 100 mM NaCl at pH 7.35, the solution was scanned immediately after the addition of 4 mM Na_2CO_3 and NaH_2PO_4.

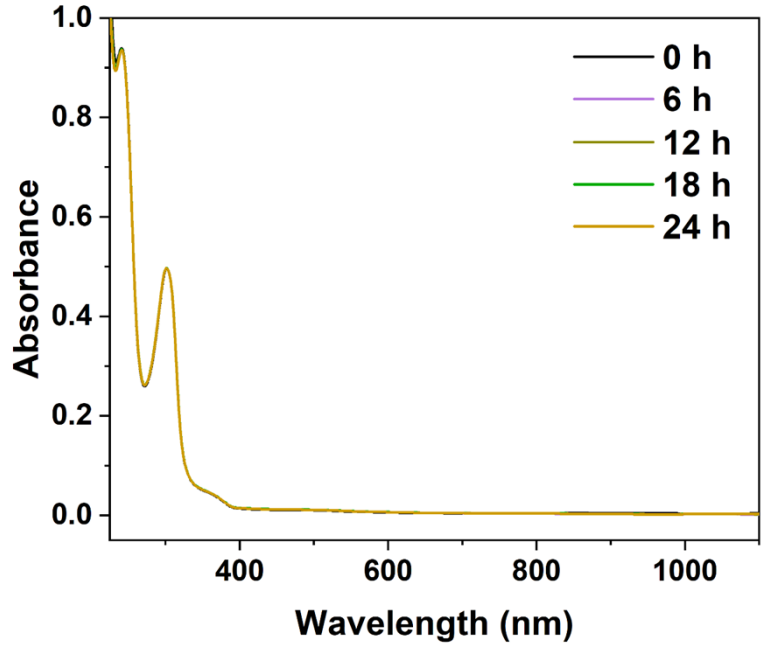

Figure S36. UV–vis spectra of a solution containing 0.10 mM of **2** in 50 mM HEPES and 100 mM NaCl at pH 7.35, the solution was scanned immediately after the addition of 4 mM Na_2CO_3 and NaH_2PO_4.

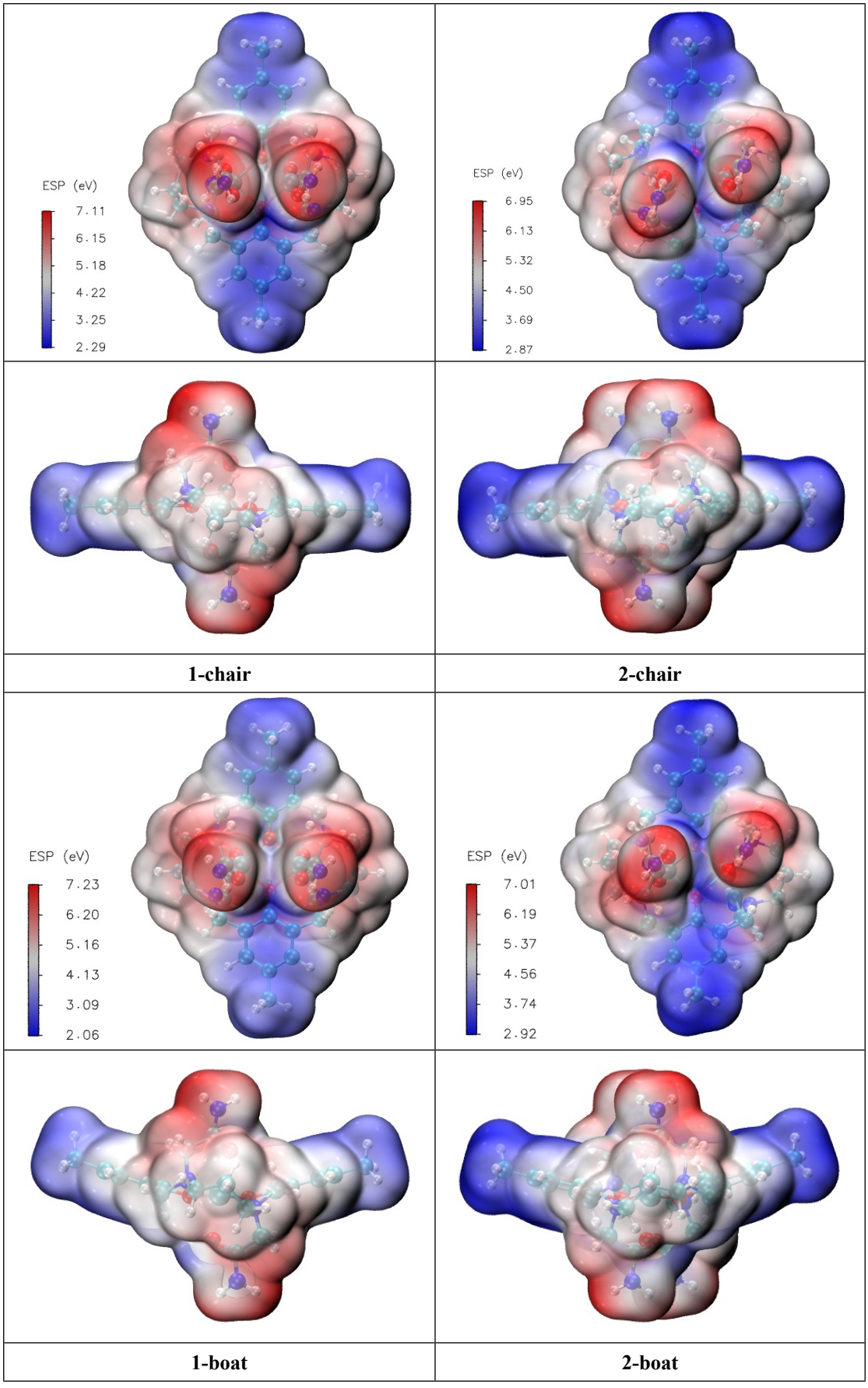

Figure S37. Electrostatic potential (ESP) map of **1** (top) and **2** (bottom). (Isovalue: 0.001 a.u.).

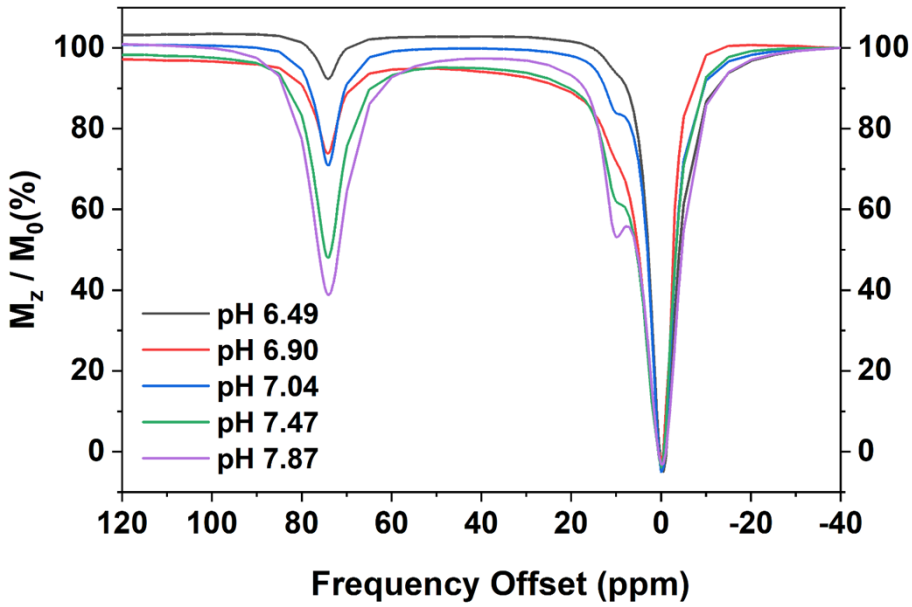

Figure S38. Variable-pH CEST spectra for 10 mM aqueous solutions of **1** with 50 mM HEPES and 100 mM NaCl (pH 6.49–7.87, see legend. 9.4 T NMR, B_1 = 20 μT×4 s, 37 °C, pH = 7.47).

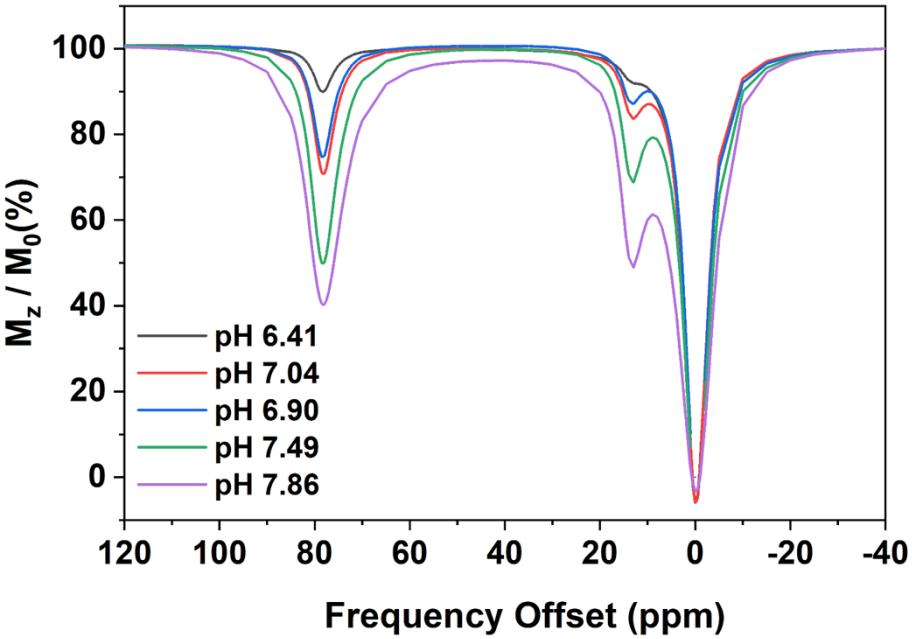

Figure S39. Variable-pH CEST spectra for 10 mM aqueous solutions of **2** with 50 mM HEPES and 100 mM NaCl (pH 6.41–7.86, see legend. 9.4 T NMR, B_1 = 20 μT×4 s, 37 °C, pH = 7.47).

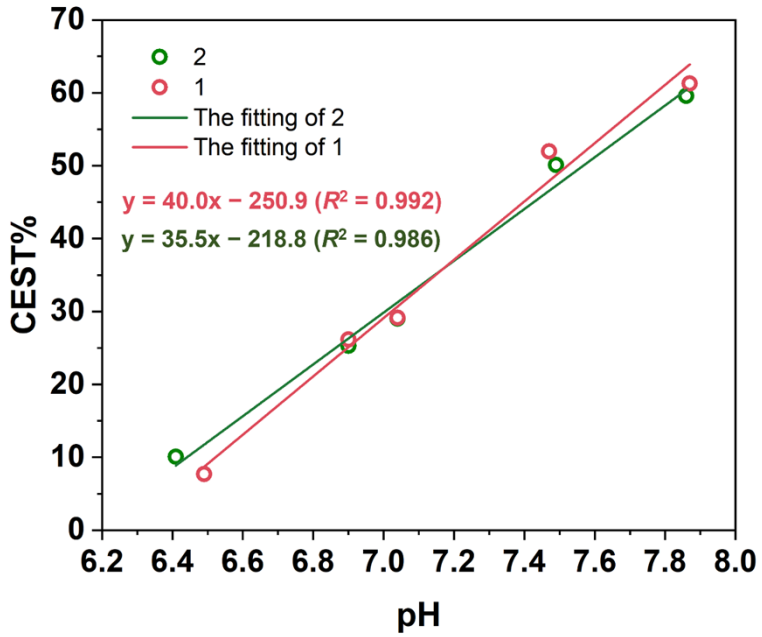

Figure S40. CEST spectra recorded at 9.4 T for 10 mM **1** (red, pH 7.46) and 10 mM **2** (green, pH 7.48) in HEPES at 37 °C, with a 4 s presaturation pulse of 20 μT.

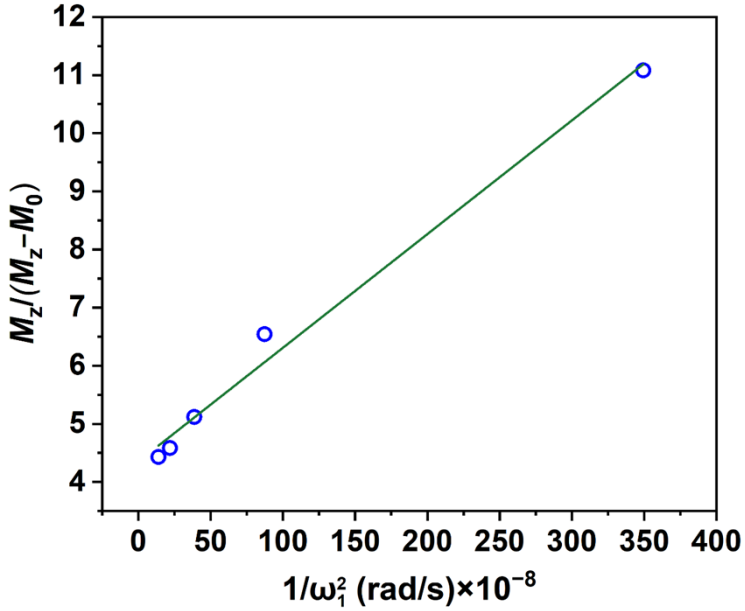

Figure S41. Omega plot of 10 mM **1** in 50 mM HEPES buffer solution at pH 6.90 and 37 ºC.

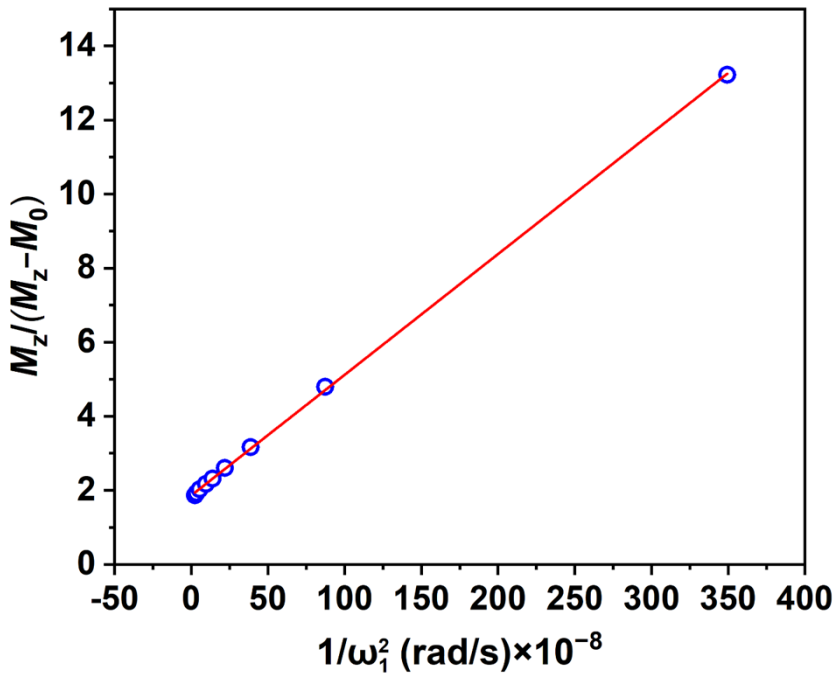

Figure S42. Omega plot of 10 mM **1** in 50 mM HEPES buffer solution at pH 7.47 and 37 ºC.

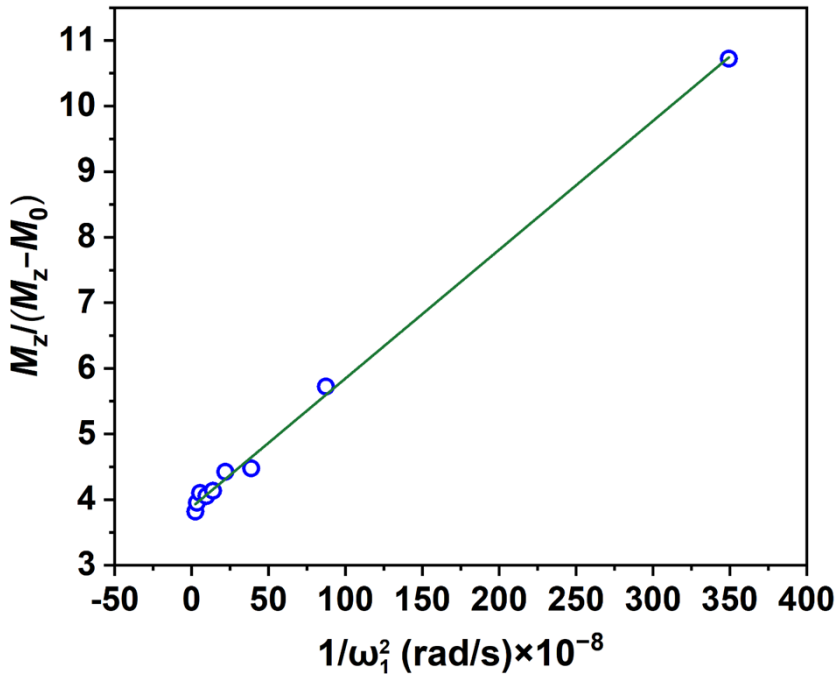

Figure S43. Omega plot of 10 mM **2** in 50 mM HEPES buffer solution at pH 6.90 and 37 ºC.

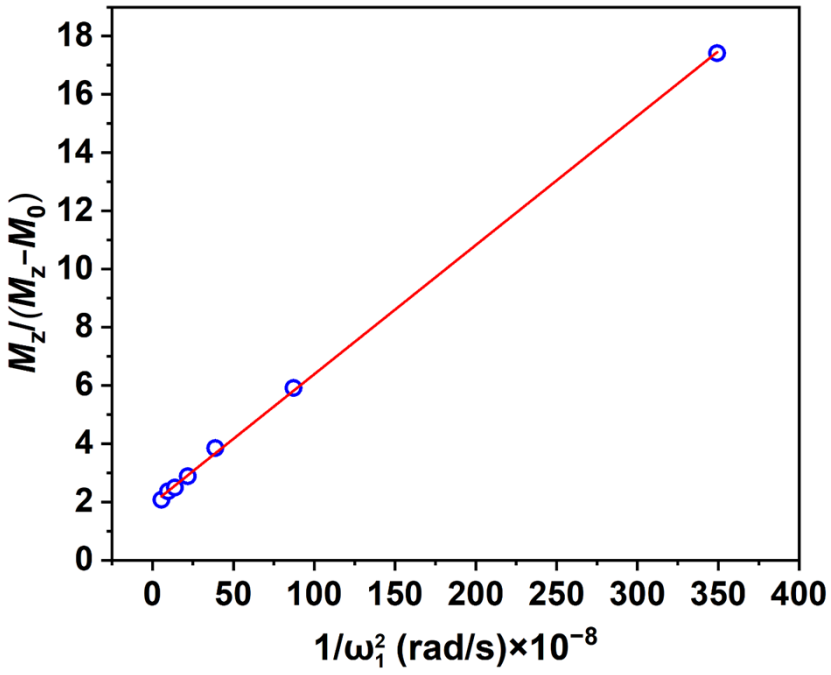

Figure S44. Omega plot of 10 mM **2** in 50 mM HEPES buffer solution at pH 7.49 and 37 ºC.

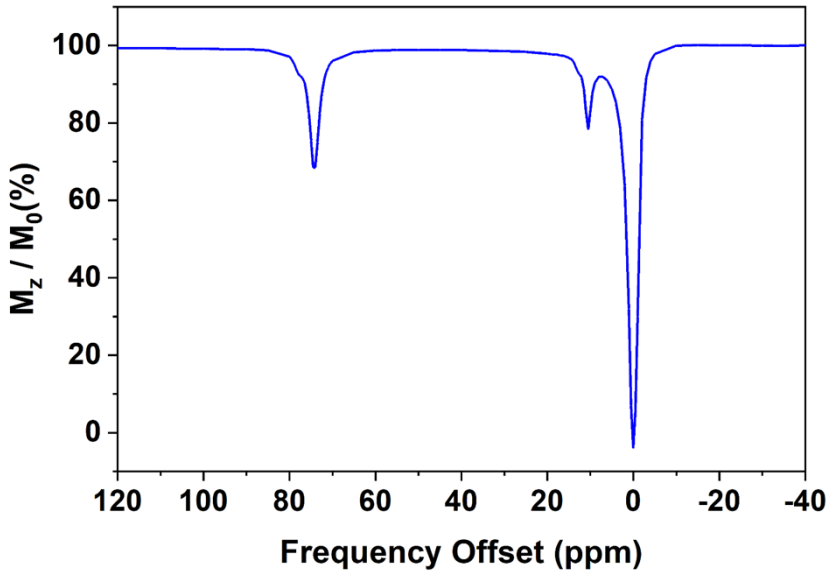

Figure 45. CEST spectra recorded at 9.4 T for 10 mM **1** (pH 7.47) in 50 mM HEPES and 100 mM NaCl buffer solution at 37 °C, with a 4 s presaturation pulse of 6 μT.

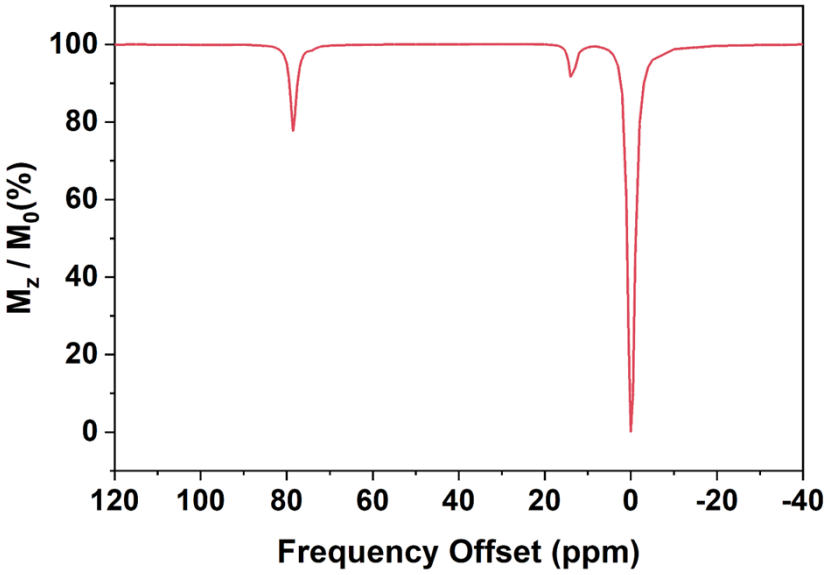

Figure 46. CEST spectra recorded at 9.4 T for 10 mM **2** (pH 7.49) in 50 mM HEPES and 100 mM NaCl buffer solution at 37 °C, with a 4 s presaturation pulse of 6 μT.

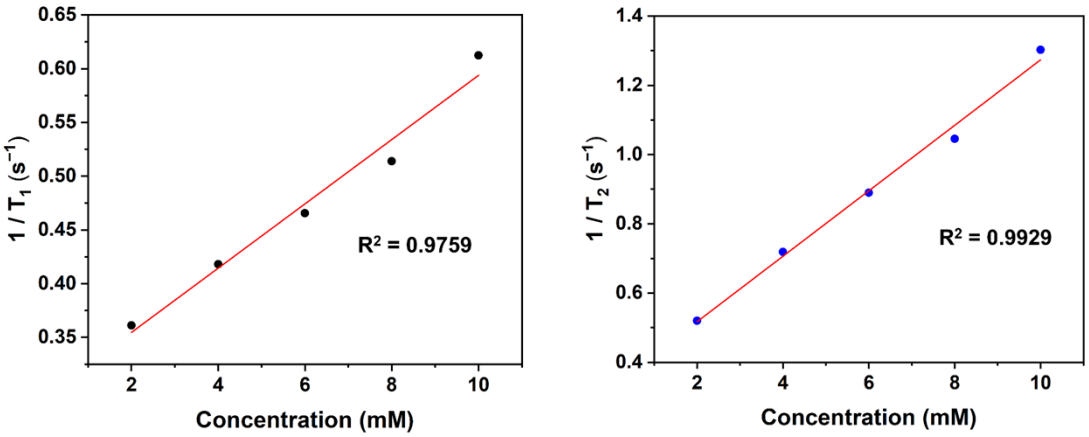

Figure S47. Plots of ($1/T_i$) versus concentration of **1**. R_1 value of 0.0299 ± 0.003 $mM^{-1}s^{-1}$ for **1** was determined, whereas R_2 value was 0.0945 ± 0.005 $mM^{-1}s^{-1}$.

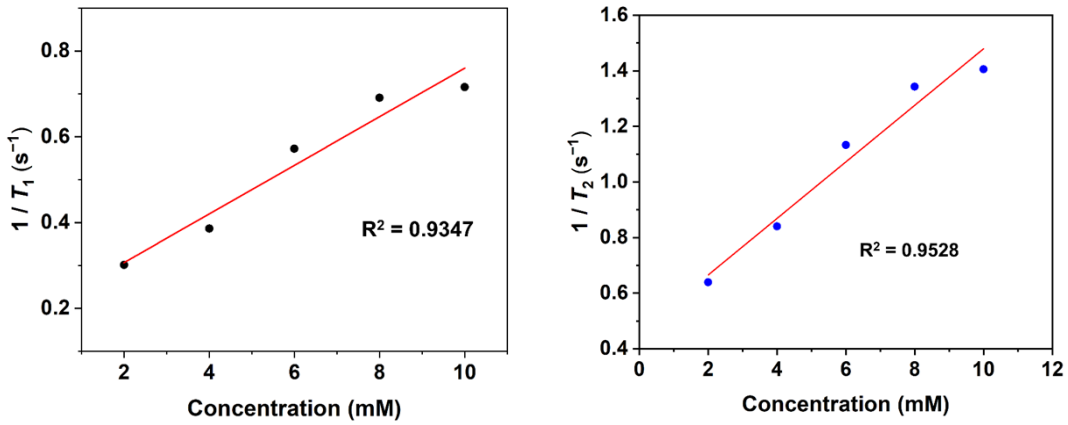

Figure S48. Plots of $(1/T_i)$ versus concentration of **2**. R_1 value of 0.0557 ± 0.007 $mM^{-1}s^{-1}$ for **2** was determined, whereas R_2 value was 0.102 ± 0.011 $mM^{-1}s^{-1}$.

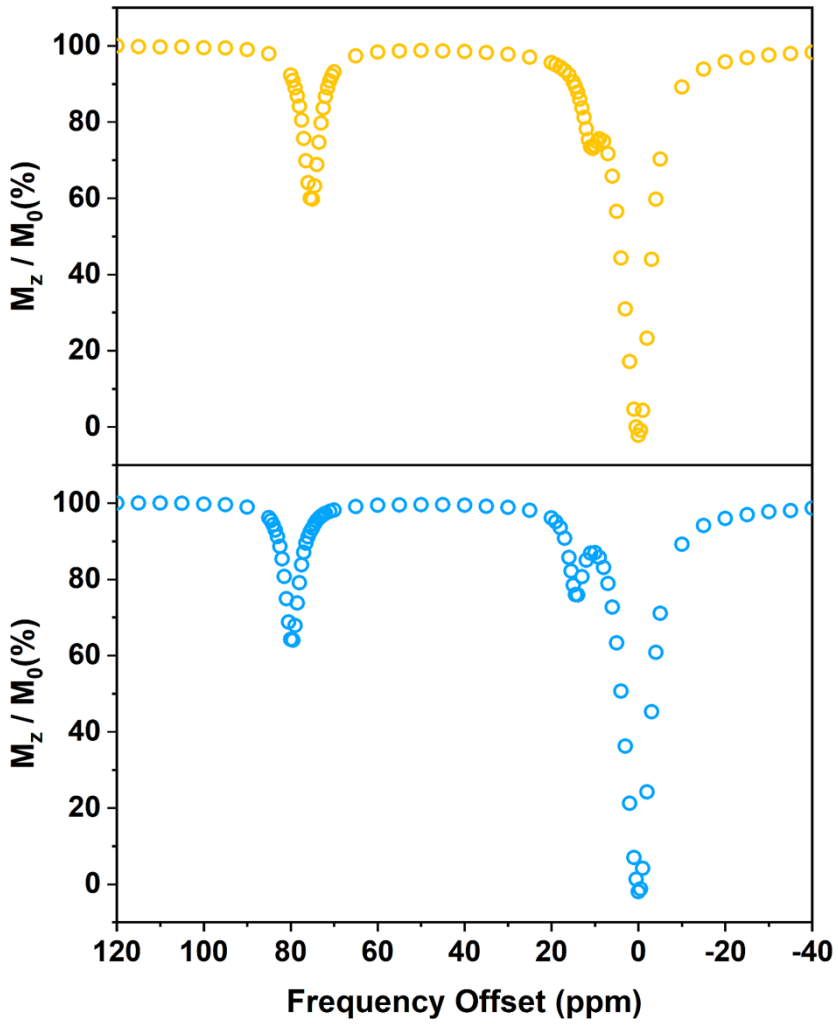

Figure S49.CEST spectra recorded at 9.4 T for 10 mM **1** (top, pH 7.46) and 10 mM **2** (bottom, pH 7.48) in FBS at 37 °C, with a 4 s presaturation pulse of 20 μT.

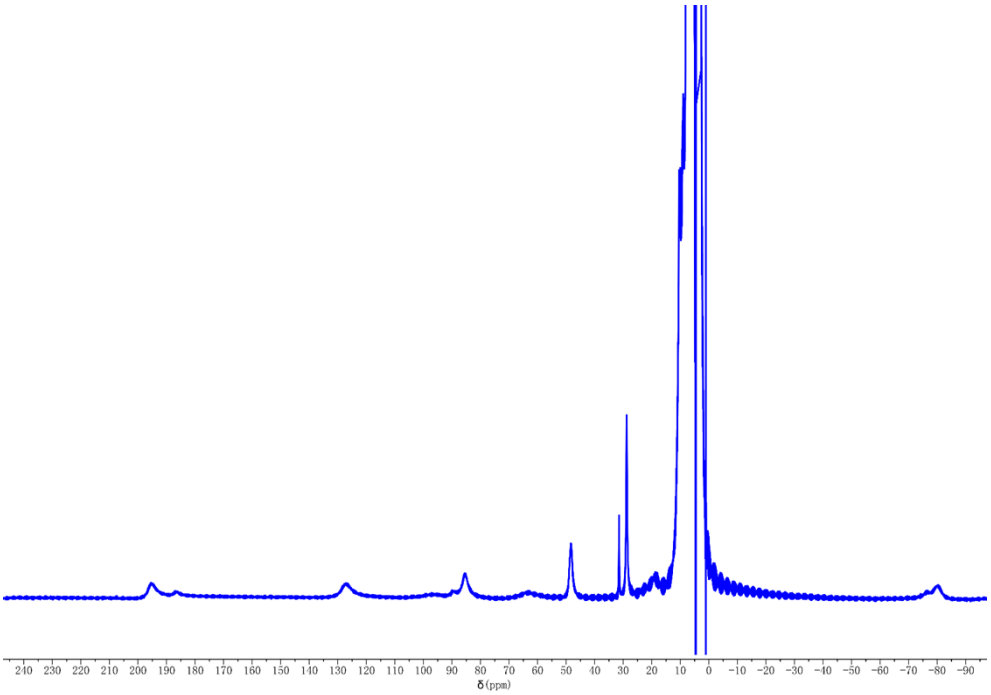

Figure S50. 400 MHz ^{1}H NMR spectra of 10 mM **1** in FBS at pH 7.50, collected at 37 °C.

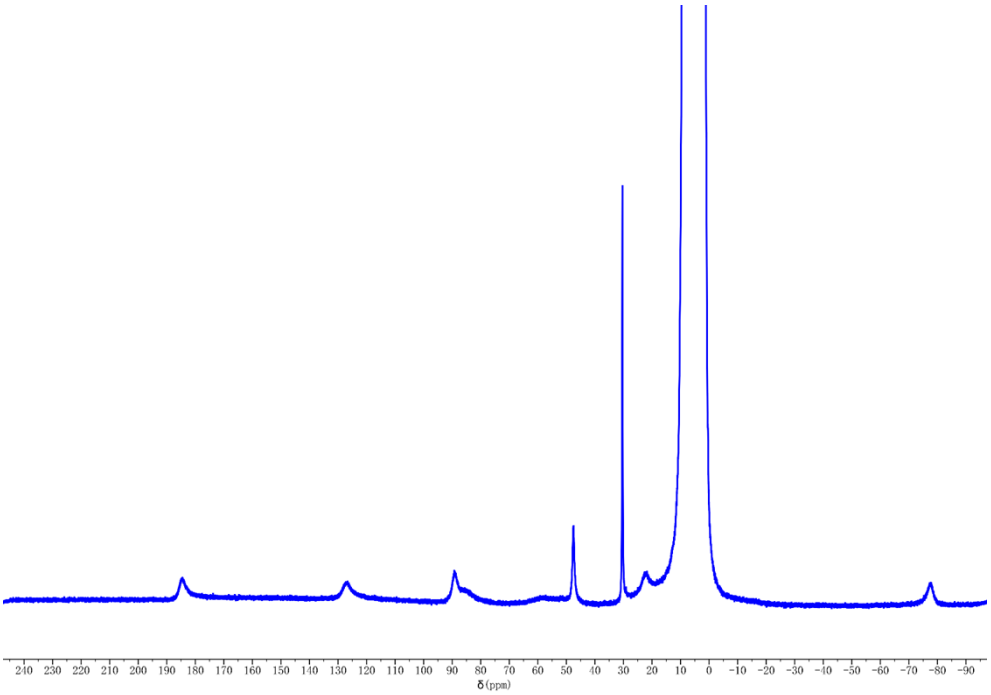

Figure S51. 400 MHz ^{1}H NMR spectra of 10 mM **2** in FBS at pH 7.51 collected at 37 °C.

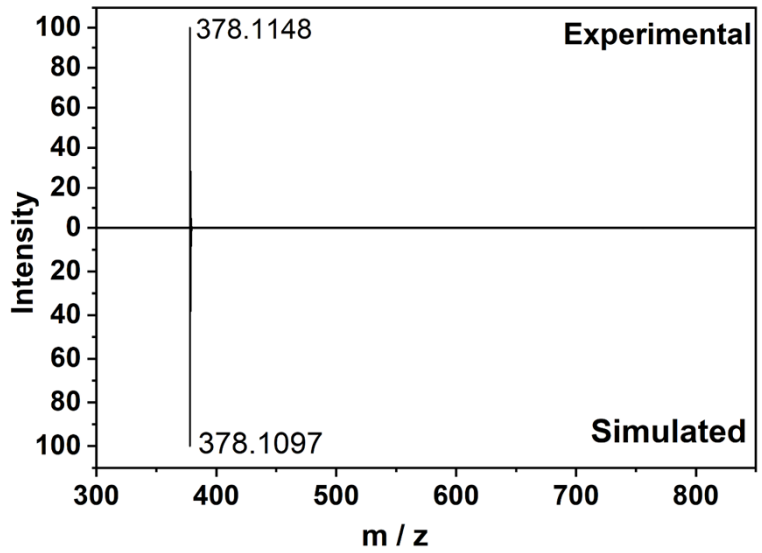

Figure S52. Mass spectrum (ESI) for **1** in MeOH. The 378.1106 m/z feature is assigned to $[L+2M+H]^{2+}$ (calculated m/z = 378.1097). The 755.2086 m/z feature is assigned to $[L+2M+2H]^{+}$ (calculated m/z = 755.2120).

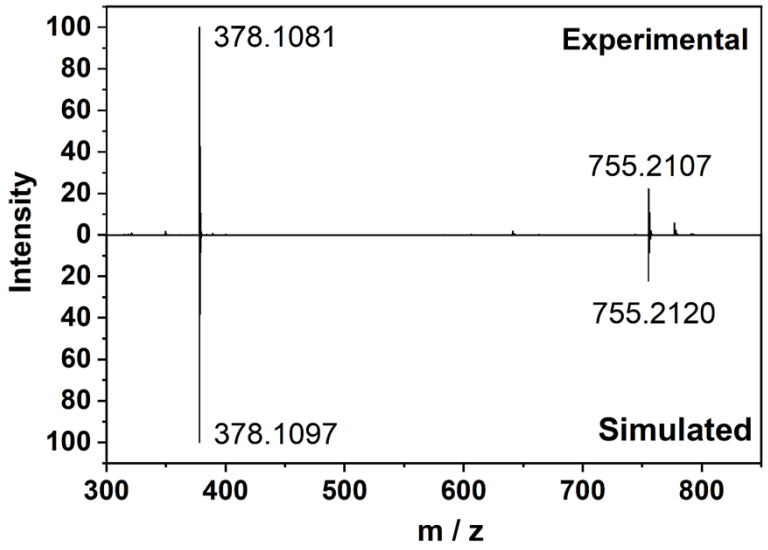

Figure S53. Mass spectrum (ESI) for **2** in MeOH. The 378.1081 m/z feature is assigned to $[L+2M+H]^{2+}$ (calculated m/z = 378.1097). The 755.2017 m/z feature is assigned to $[L+2M+2H]^{+}$ (calculated m/z = 755.2120).

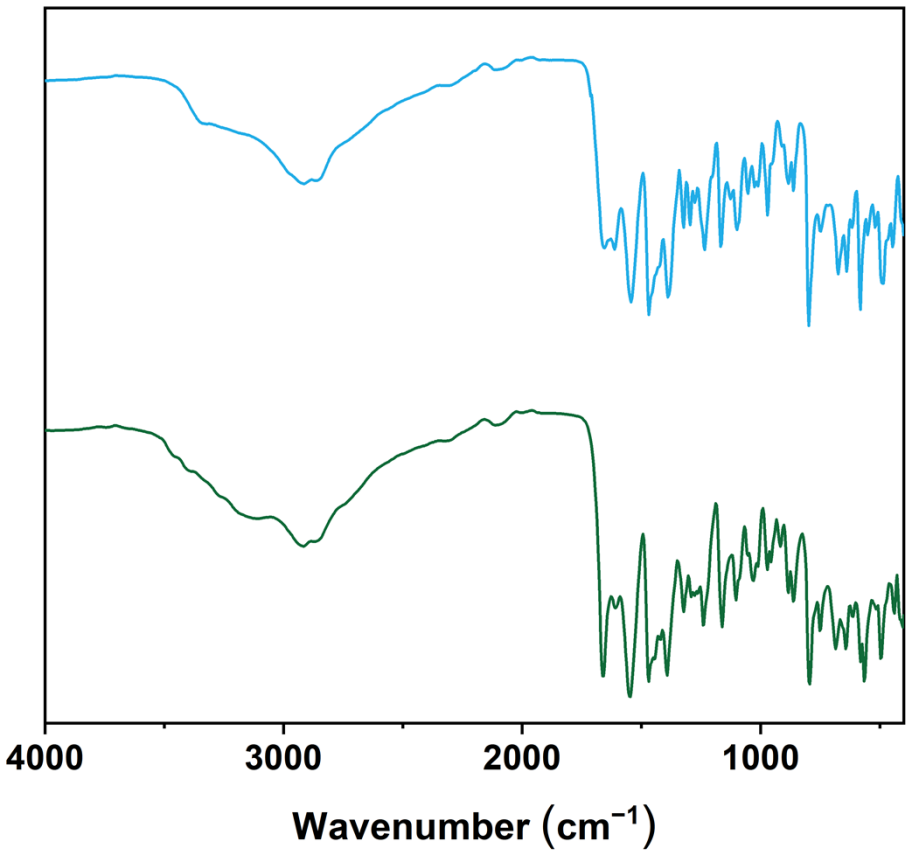

Figure S54. IR spectra of solid-state samples of **1** (blue) and **2** (green).

References

1 G. M. Sheldrick, Crystal structure refinement with SHELXL, *Acta Cryst.*, 2015, **C71**, 3–8.

2 O. V. Dolomanov, L. J. Bourhis, R. J. Gildea, J. A. K. Howard and H. Puschmann, OLEX2: a complete structure solution, refinement and analysis program, *J. Appl. Cryst.*, 2009, **42**, 339–341.

3 D. F. Evans, 400. The determination of the paramagnetic susceptibility of substances in solution by nuclear magnetic resonance, *J. Chem. Soc.*, 1959, **81**, 2003–2005.

4 D. Montagner, V. Gandin, C. Marzano and A. Erxleben, Phosphate Diester Cleavage, DNA Interaction and Cytotoxic Activity of a Bimetallic Bis(1,4,7-triazacyclononane) Zinc Complex (Eur. J. Inorg. Chem. 25/2014), *Eur. J. Inorg. Chem.*, 2014, **2014**, 4043–4049.

5 G. A. Bain and J. F. Berry, Diamagnetic Corrections and Pascal's Constants, *J. Chem. Educ.*, 2008, **85**, 532–536.

6 A. Brajter-Toth, Electrochemistry for Chemists, 2nd ed By Donald Sawyer (Texas A&M University), Andrzej Sobkowiak (Rzeszow University of Technology), and Julian L. Roberts, Jr. (University of Redlands). Wiley: New York. 1995. xv + 505 pp. $64.95. ISBN 0-471-59468-7, *J. Am. Chem. Soc.*, 1996, **118**, 10339–10340.

7 N. Frank, The ORCA program system, *WIREs Comput. Mol. Sci.*, 2012, **2**, 73–78.

8 N. Frank, Software update: the ORCA program system, version 4.0, *WIREs Comput. Mol. Sci.*, 2018, **8**, e1327.

9 F. Neese, F. Wennmohs, U. Becker and C. Riplinger, The ORCA quantum chemistry program package, *J. Chem. Phys.*, 2020, **152**, 224108.

10 M. Garcia-Ratés and F. Neese, Effect of the Solute Cavity on the Solvation Energy and its Derivatives within the Framework of the Gaussian Charge Scheme, *J. Comput. Chem.*, 2020, **41**, 922–939.

11 E. Caldeweyher, C. Bannwarth and S. Grimme, Extension of the D3 dispersion coefficient model, *J. Chem. Phys.*, 2017, **147**, 034112.

12 S. Grimme, C. Bannwarth and P. Shushkov, A Robust and Accurate Tight-Binding Quantum Chemical Method for Structures, Vibrational Frequencies, and Noncovalent Interactions of Large Molecular Systems Parametrized for All spd-Block Elements (Z = 1–86), *J. Chem. Theory Comput.*, 2017, **13**, 1989–2009.

13 B. J. Berne, G. Ciccotti and D. F. Coker, *Classical and Quantum Dynamics in Condensed Phase Simulations*, World Scientific Publishing Company, 1998.

14 G. Henkelman and H. Jónsson, Improved tangent estimate in the nudged elastic band method for finding minimum energy paths and saddle points, *J. Chem. Phys.*, 2000, **113**, 9978–9985.

15 E. v. Lenthe, E. J. Baerends and J. G. Snijders, Relativistic regular two-component Hamiltonians, *J. Chem. Phys.*, 1993, **99**, 4597–4610.

16 F. Neese, F. Wennmohs, A. Hansen and U. Becker, Efficient, approximate and parallel Hartree–Fock and hybrid DFT calculations. A 'chain-of-spheres' algorithm for the Hartree–Fock exchange, *Chem. Phys.*, 2009, **356**, 98–109.

17 K. Eichkorn, O. Treutler, H. Öhm, M. Häser and R. Ahlrichs, Auxiliary basis sets to approximate Coulomb potentials, *Chem. Phys. Lett.*, 1995, **240**, 283–290.

18 K. Eichkorn, F. Weigend, O. Treutler and R. Ahlrichs, Auxiliary basis sets for main row atoms and transition metals and their use to approximate Coulomb potentials, *Theor.*

Chem. Acc., 1997, **97**, 119–124.

19 A. P. Ginsberg, Magnetic exchange in transition metal complexes. 12.[1] Calculation of cluster exchange coupling constants with the Xα-scattered wave method, *J. Am. Chem. Soc.*, 1980, **102**, 111–117.

20 J. K. S. Wan, J. Dobkowski and N. J. Turro, Time-resolved ESR studies of triplet energy transfer and triplet properties of some model bromo-substituted naphthalene compounds at 77 K, *Chem. Phys. Lett.*, 1986, **131**, 129–133.

21 A. Bencini and D. Gatteschi, Xα-SW Calculations of the Electronic Structure and Magnetic Properties of Weakly Coupled Transition-Metal Clusters. The $[Cu_2Cl_6]^{2-}$ Dimers, *J. Am. Chem. Soc.*, 1986, **108**, 5763–5771.

22 T. Soda, Y. Kitagawa, T. Onishi, Y. Takano, Y. Shigeta, H. Nagao, Y. Yoshioka and K. Yamaguchi, Ab initio computations of effective exchange integrals for H–H, H–He–H and Mn2O2 complex: comparison of broken-symmetry approaches, *Chem. Phys. Lett.*, 2000, **319**, 223–230.

23 X. Guo, L. Zhang, J. Hu, B. Szilágyi, M. Yu, S. Chen, G. Tircsó, X. Zhou and J. Tao, Chem. Sci., *Chem. Sci.*, 2023, **14**, 14157–14165.

24 A. E. Thorarinsdottir, K. Du, J. H. P. Collins and T. D. Harris, Ratiometric pH Imaging with a Co^{II2} MRI Probe via CEST Effects of Opposing pH Dependences, *J. Am. Chem. Soc.*, 2017, **139**, 15836–15847.

25 A. E. Thorarinsdottir, S. M. Tatro and T. D. Harris, Electronic Effects of Ligand Substitution in a Family of $Co^{II\,2}$ PARACEST pH Probes, *Inorg. Chem.*, 2018, **57**, 11252–11263.

26 A. E. Thorarinsdottir and T. D. Harris, Dramatic enhancement in pH sensitivity and signal intensity through ligand modification of a dicobalt PARACEST probe, *Chem. Commun.*, 2019, **55**, 794–797.

27 C. J. Bond, R. Cineus, A. Y. Nazarenko, J. A. Spernyak and J. R. Morrow, Isomeric Co(II) paraCEST agents as pH responsive MRI probes, *Dalton Trans.*, 2020, **49**, 279–284.

28 S. J. Dorazio, A. O. Olatunde, J. A. Spernyak and J. R. Morrow, CoCEST: cobalt(II) amide-appended paraCEST MRI contrast agents, *Chem. Commun.*, 2013, **49**, 10025–10027.

29 S. J. Dorazio, A. O. Olatunde, P. B. Tsitovich and J. R. Morrow, Comparison of divalent transition metal ion paraCEST MRI contrast agents, *J. Biol. Inorg. Chem.*, 2014, **19**, 191–205.

30 A. O. Olatunde, J. M. Cox, M. D. Daddario, J. A. Spernyak, J. B. Benedict and J. R. Morrow, Seven-coordinate Co(II), Fe(II) and six-coordinate Ni(II) amide-appended macrocyclic complexes as ParaCEST agents in biological media, *Inorg. Chem.*, 2014, **53**, 8311–8321.

31 A. O. Olatunde, S. J. Dorazio, J. A. Spernyak and J. R. Morrow, The NiCEST Approach: Nickel(II) ParaCEST MRI Contrast Agents, *J. Am. Chem. Soc.*, 2012, **134**, 18503–18505.

32 A. O. Olatunde, C. J. Bond, S. J. Dorazio, J. M. Cox, J. B. Benedict, M. D. Daddario, J. A. Spernyak and J. R. Morrow, Six, Seven or Eight Coordinate Fe^{II}, Co^{II} or Ni^{II} Complexes of Amide-Appended Tetraazamacrocycles for ParaCEST Thermometry, *Chem. – Eur. J.*, 2015, **21**, 18290–18300.

33 P. J. Burns, J. M. Cox and J. R. Morrow, Imidazole-Appended Macrocyclic Complexes of

Fe(II), Co(II), and Ni(II) as ParaCEST Agents, *Inorg. Chem.*, 2017, **56**, 4545–4554.

34 R. N. Pradhan, S. Chakraborty, P. Bharti, J. Kumar, A. Ghosh and A. K. Singh, Seven coordinate Co(II) and six coordinate Ni(II) complexes of an aromatic macrocyclic triamide ligand as paraCEST agents for MRI, *Dalton Trans.*, 2019, **48**, 8899–8910.

35 P. B. Tsitovich, J. A. Spernyak and J. R. Morrow, A Redox-Activated MRI Contrast Agent that Switches Between Paramagnetic and Diamagnetic States, *Angew. Chem. Int. Ed.*, 2013, **52**, 13997–14000.

36 K. Du, A. E. Thorarinsdottir and T. D. Harris, Selective Binding and Quantitation of Calcium with a Cobalt-Based Magnetic Resonance Probe, *J. Am. Chem. Soc.*, 2019, **141**, 7163–7172.

37 W. S. Fernando, A. F. Martins, P. Zhao, Y. Wu, G. E. Kiefer, C. Platas-Iglesias and A. D. Sherry, Breaking the Barrier to Slow Water Exchange Rates for Optimal Magnetic Resonance Detection of paraCEST Agents, *Inorg. Chem.*, 2016, **55**, 3007–3014.

38 Z. Garda, V. Nagy, A. Rodríguez-Rodríguez, R. Pujales-Paradela, V. Patinec, G. Angelovski, É. Tóth, F. K. Kálmán, D. Esteban-Gómez, R. Tripier, C. Platas-Iglesias and G. Tircsó, Unexpected Trends in the Stability and Dissociation Kinetics of Lanthanide(III) Complexes with Cyclen-Based Ligands across the Lanthanide Series, *Inorg. Chem.*, 2020, **59**, 8184–8195.

39 S. Aime, A. Barge, D. Delli Castelli, F. Fedeli, A. Mortillaro, F. U. Nielsen and E. Terreno, Paramagnetic Lanthanide(III) complexes as pH-sensitive chemical exchange saturation transfer (CEST) contrast agents for MRI applications, *Magn. Reson. Med.*, 2002, **47**, 639–648.

40 T. Gambino, L. Valencia, P. Pérez-Lourido, D. Esteban-Gómez, M. Zaiss, C. Platas-Iglesias and G. Angelovski, Inert macrocyclic Eu3+ complex with affirmative paraCEST features, *Inorg. Chem. Front.*, 2020, **7**, 2274–2286.

41 P. Pietrzyk, M. Srebro, M. Radoń, Z. Sojka and A. Michalak, Spin Ground State and Magnetic Properties of Cobalt(II): Relativistic DFT Calculations Guided by EPR Measurements of Bis(2,4-acetylacetonate)cobalt(II)-Based Complexes, *J. Phys. Chem. A*, 2011, **115**, 2316–2324.